



# A SPH-based numerical study of the crack arrest behaviour of rubber toughened PMMA under impact loading

K. S. Tan · P. Longere · N. M. Jali

Received: 19 May 2021 / Accepted: 4 January 2022 / Published online: 24 January 2022  
© The Author(s), under exclusive licence to Springer Nature B.V. 2022

**Abstract** The objective of the present work is to propose an engineering-oriented numerical methodology capable of reproducing crack initiation and arrest in semi-brittle structures under high loading rate. With this aim in view, the SPH-based method implemented in LS-DYNA is employed to reproduce the three-dimensional crack initiation, propagation and arrest in a rate- and temperature-dependent grade of RT-PMMA under Kalthoff and Winkler-type impact loading. The ability of critical maximum principal stress- and critical plastic strain-controlled failure criteria, first individually and then combined to reproduce the crack arrest was evaluated by comparison with experimental results. In spite of the overall brittle nature of the PMMA matrix, it was shown that the most pertinent criterion for the material of interest is the one expressed in terms of critical plastic strain, as a consequence of the gain in ductility brought by the embedded rubber nanoparticles. In practice, the real crack pattern can be reproduced only if the two criteria are used together. Following a design of experiment, an optimised set of values for the critical maximum

principal stress and plastic failure strain were found. A good agreement in terms of crack advance (as a function of the impact velocity) and propagation angle is seen between the experimental and numerical results.

**Keywords** RT-PMMA · Brittle fracture · Crack propagation · Crack arrest · Kalthoff–Winkler experiment · SPH method

## 1 Introduction

While PMMA presents advantages in terms of transparency, weather resistance and processing conditions, it is also known for its low toughness. Yet, the addition of rubber nanoparticles inside a PMMA matrix has proven to significantly increase the toughness of the resulting composite material known as rubber-toughened PMMA or RT-PMMA, see e.g. Milios et al. (1986), Lalande et al. (2006), Mazidi et al. (2018), and Wang et al. (2019). This gain in ‘ductility’ is increasing with increasing rubber nanoparticle concentration. This effect is also visible in terms of impact resistance, as shown by Mat Jali and Longère (2020a, b) who carried out Kalthoff and Winkler (KW)-type impact tests at various impact velocities on a class of RT-PMMA with different rubber nanoparticle concentrations. KW-type impacts consist of

---

K. S. Tan · N. M. Jali  
Faculty of Engineering, National Defence University of Malaysia, 57000 Kuala Lumpur, Malaysia

P. Longere (✉)  
Institut Clément Ader, Université de Toulouse, ISAE-SUPAERO, MINES ALBI, UPS, INSA, CNRS, 31400 Toulouse, France  
e-mail: patrice.longere@isae-supero.fr

impacting the edge of a doubly-notched plate made of the material of interest in view of investigating the conditions for crack initiation and propagation under high loading rate, see Kalthoff and Winkler (1987), Kalthoff (1988), Zhou et al. (1996a) and Ravi-Chandar et al. (2000). Mat Jali and Longère (2020a, b) notably showed that the higher the rubber nanoparticle concentrations, the higher the resistance to crack propagation. For the highest rubber nanoparticle concentration, within an impact velocity range, the crack is even seen to arrest inside the specimen.

KW-type impact test has been, historically, a discriminating case for evaluating the performances of numerical methods aimed at reproducing the dynamic crack growth and its consequences in brittle vs. ductile structures. Among the most representative attempts, one can cite those based on the finite element method (FEM), as notably done in two then three dimensions by Needleman and Tvergaard (1995), Zhou et al. (1996b), Batra and Gummalla (2000), Batra and Ravinsankar (2000), Batra and Lear (2004), and more recently by Li et al. (2016) who applied a phase field-based approach to regularise the crack-induced singularity. While bringing a better understanding of the mechanisms leading to the more or less progressive ruin of the structure, they all required a very fine meshing of the area around the notch tip (during the whole crack propagation) and leads to an unavoidable dependence of the crack path on the meshing (size and orientation) whatever the adopted crack representation (element deletion/erosion, node-splitting, etc.). To partly alleviate these issues, some authors took advantage of the extended FEM (XFEM) which consists of embedding the crack within the finite element and describing the kinematic consequences of the crack through additional nodal degrees of freedom. In this context, one can notably cite the two-dimensional approaches by Song et al. (2006), Combescure et al. (2012) and Haboussa et al. (2012). The results are convincing but the XFEM remains very cumbersome to implement in commercial FE codes (the versions by default being often very limited) and is also expensive in terms of computation time. Mesh-free methods seem more efficient and less time consuming to deal with fracture, and in particular with brittle fracture, given that the a priori knowledge of the crack path is not required. In this line, Li et al. (2002) conducted mesh-free Galerkin simulation of the KW-type impact test while Raymond et al. (2014)

used the smooth particle hydrodynamics (SPH)-based method to do the same, both with also convincing results. One can also cite numerical simulations using peridynamics-based methods, see e.g. Zhou et al. (2016). Yet, the common point to the above mentioned simulations is that they mostly aim at reproducing qualitatively experimental trends while rarely comparing quantitatively their numerical results with experimental ones. In particular, in the case of brittle fracture, none show results with crack arrest (i.e. involving finite crack advance), which constitutes a genuine numerical challenge.

The objective of the present work is to propose an engineering-oriented numerical methodology capable of reproducing crack initiation and arrest in semi-brittle structures under high loading rate with an application to RT-PMMA, see Kobayashia and Mall (1979) for the concept of crack arrest. For that purpose, the SPH-based method is employed to reproduce the three-dimensional crack initiation, propagation and arrest in a semi-brittle rate- and temperature-dependent grade of RT-PMMA using the commercial explicit computation code LS-DYNA.

In Sect. 2, some fracture mechanics-related results about crack propagation under shear loading are recalled as well as some salient experimental results about the high loading rate resistance under KW-type impact of a commercial RT-PMMA, viz. RT-PMMA100, exhibiting crack arrest within an impact velocity range. Section 3 is dedicated to the SPH related-numerical procedure with attention paid to the spatial discretisation, materials definition, formulation type and contact conditions. The preliminary numerical analysis of the KW-type impact test in Sect. 4 aims at evaluating the ability of stress- and strain-dependent failure criteria to reproduce, first individually and then combined, the crack initiation and arrest in the material of interest. Following a design of experiment, a set of parameters is identified and applied to the RT-PMMA100 in Sect. 5 leading to a very good agreement between numerical and experimental results. Concluding remarks and perspectives are given in Sect. 6.

## 2 Theoretical background and experimental results

KW impact test, see Kalthoff and Winkler (1987), consists of impacting the edge of a doubly-prenotched plate made of the material of interest by a cylindrical projectile. The impact of the projectile between the two notches induces a quasi pure Mode II type loading at the notches tips, at least as long as the waves reflected from the specimen boundaries do not interact and involve a complex loading and further mixed mode of crack propagation, see Ravi-Chandar et al. (2000). Depending on the material and impact velocity, the authors reported either a crack kink angle close to  $-70^\circ$  they ascribed to brittle failure or a self-similar crack propagation ('kink' angle of  $0^\circ$ ) they ascribed to ductile failure (actually resulting from a form of dynamic strain localization known as adiabatic shear banding, see e.g. Roux et al. (2015) and Manar and Longère (2019). A second bifurcation is sometimes observed, see Zhou et al. (1996a).

In this Section, some fracture mechanics-based theoretical results concerning the crack bifurcation under shear loading on the one hand, and some experimental results obtained from impact tests carried out on KW-type specimens made of the semi-ductile RT-PMMA of interest, viz. RT-PMMA100, and further used for the numerical simulations, on the other hand, are recalled.

### 2.1 Approaches of crack bifurcation under shear loading

For a  $2a$ -length crack submitted to an in-plane shear stress  $\sigma_{xy} = \tau$  loading, stress intensity factors  $K_I$  and  $K_{II}$  at the crack tips take the expressions

$$\begin{cases} K_I = 0 \\ K_{II} = \tau\sqrt{\pi a} \end{cases} \quad (1)$$

We now examine the direction of propagation of this pre-crack following two well-known theories.

#### 2.1.1 Maximum hoop stress theory

The classical maximum hoop stress theory, see e.g. Zehnder (2012), states that the crack propagation angle  $\theta^*$  obeys

$$\frac{\partial \sigma_{\theta\theta}}{\partial \theta} = 0 \quad \& \quad \frac{\partial^2 \sigma_{\theta\theta}}{\partial \theta^2} < 0 \quad \text{at } \theta = \theta^* \quad (2)$$

with

$$\begin{cases} \sigma_{\theta\theta} = \frac{1}{\sqrt{2\pi r}} \frac{1}{4} \left[ K_I \left( \cos \frac{3\theta}{2} + 3 \cos \frac{\theta}{2} \right) - 3K_{II} \left( \sin \frac{\theta}{2} + \sin \frac{3\theta}{2} \right) \right] \\ \frac{\partial \sigma_{\theta\theta}}{\partial \theta} = -\frac{1}{\sqrt{2\pi r}} \frac{3}{4} \cos \frac{\theta}{2} [K_I \sin \theta + K_{II}(3 \cos \theta - 1)] \\ \frac{\partial^2 \sigma_{\theta\theta}}{\partial \theta^2} = -\frac{1}{\sqrt{2\pi r}} \frac{3}{4} \left\{ K_I \left[ \frac{1}{2} \sin \theta \sin \frac{\theta}{2} + \cos \theta \cos \frac{\theta}{2} \right] \right. \\ \left. + K_{II} \left[ \frac{1}{2} \sin \frac{\theta}{2} (3 \cos \theta - 1) - 3 \sin \theta \cos \frac{\theta}{2} \right] \right\} \end{cases} \quad (3)$$

Accounting for (1), the set of Eq. (3) reduces to

$$\begin{cases} \sigma_{\theta\theta} = -\frac{K_{II}}{\sqrt{2\pi r}} \frac{3}{4} \left( \sin \frac{\theta}{2} + \sin \frac{3\theta}{2} \right) \\ \frac{\partial \sigma_{\theta\theta}}{\partial \theta} = -\frac{K_{II}}{\sqrt{2\pi r}} \frac{3}{4} \cos \frac{\theta}{2} (3 \cos \theta - 1) \\ \frac{\partial^2 \sigma_{\theta\theta}}{\partial \theta^2} = -\frac{K_{II}}{\sqrt{2\pi r}} \frac{3}{4} \left[ \frac{1}{2} \sin \frac{\theta}{2} (3 \cos \theta - 1) - 3 \sin \theta \cos \frac{\theta}{2} \right] \end{cases} \quad (4)$$

Applying (2)<sub>1</sub> to (4)<sub>2</sub> yields

$$\begin{cases} \cos \frac{\theta^*}{2} = 0 \rightarrow \theta^* = \pm \pi \\ 3 \cos \theta^* - 1 = 0 \end{cases} \quad (5)$$

Solution (5)<sub>1</sub> is clearly irrelevant. Accounting for (1), condition (5)<sub>2</sub> reduces to

$$\theta^* = \pm 70.56^\circ \quad (6)$$

Condition (2)<sub>2</sub> with (6) is verified for  $\theta^* = -70.56^\circ$ . The crack starts to propagate at the kink angle  $\theta^*$  as soon as the hoop stress reaches the critical stress  $\sigma_c$ :

$$\sigma_{\theta\theta}(\theta^*) = \sigma_c = \frac{K_{Ic}}{\sqrt{\pi a}} \quad (7)$$

where  $K_{Ic}$  represents the critical stress intensity factor. Accounting for (4)<sub>1</sub>, (7) reads

$$-\frac{3}{4} K_{II} \left( \sin \frac{\theta^*}{2} + \sin \frac{3\theta^*}{2} \right) = K_{Ic} \quad (8)$$

Injecting the value  $\theta^* = -70.56^\circ$  into (8) yields  $K_{II} = 0.87K_{Ic}$ .

2.1.2 Minimum strain energy density theory

The minimum strain energy density theory, see Sih (1974, 1991), states that the crack propagation angle  $\theta^*$  obeys

$$\frac{\partial S(\theta)}{\partial \theta} = 0 \ \& \ \frac{\partial^2 S(\theta)}{\partial \theta^2} > 0 \ \text{at} \ \theta = \theta^* \tag{9}$$

where the strain energy density  $S(\theta)$  is expressed by

$$S(\theta) = \frac{a_{11}K_I^2 + 2a_{12}K_I K_{II} + a_{22}K_{II}^2}{16\pi\mu} \tag{10}$$

with

$$\begin{cases} a_{11} = (K - \cos \theta)(1 + \cos \theta) \\ a_{22} = (K + 1)(1 - \cos \theta) + (1 + \cos \theta)(3 \cos \theta - 1) \\ a_{12} = (2 \cos \theta - K + 1) \sin \theta \end{cases} \tag{11}$$

and

$$K = \begin{cases} 3 - 4\nu \ \text{in plane strain} \\ \frac{3 - \nu}{1 + \nu} \ \text{in plane stress} \end{cases} \tag{12}$$

Accounting for (1), (10) reduces to

$$S(\theta) = \frac{a_{22}K_{II}^2}{16\pi\mu} = \frac{a_{22}\sigma^2 a}{16\mu} \tag{13}$$

Conditions (9)<sub>1,2</sub> accordingly become

$$\begin{cases} \frac{\partial a_{22}}{\partial \theta} = \sin \theta (K - 1 - 6 \cos \theta) = 0 \\ \frac{\partial^2 a_{22}}{\partial \theta^2} = \cos \theta (K - 1 - 6 \cos \theta) + 6 \sin^2 \theta > 0 \end{cases} \tag{14}$$

yielding

$$\begin{cases} \theta^* = 0 \ \text{self - similar crack propagation} \\ \cos \theta^* = \frac{K - 1}{6} \ \text{crack bifurcation} \end{cases} \tag{15}$$

Solution (15)<sub>1</sub> does not verify condition (14)<sub>2</sub> for real materials. Under the plane strain assumption, see (12)<sub>1</sub>, (15)<sub>2</sub> reads

$$\cos \theta^* = \frac{1 - 2\nu}{3} \tag{16}$$

Together with condition (14)<sub>2</sub>, (16) implies  $\theta^* = -70.56^\circ$  for  $\nu = 0$  which matches with the value derived from the maximum hoop stress theory, see (6). For  $\nu = 1/3$ , we have  $\cos \theta^* = \frac{1}{9}$  and then  $\theta^* = -83.62^\circ$ .

2.1.3 Expected propagation angle during KW impact tests

If under pure Mode I loading, the crack propagates in a self-similar way ( $\theta^* = 0^\circ$ ), pure Mode II loading induces a crack bifurcation. As above shown, according to the maximum hoop stress theory, the expected kink angle under pure Mode II is close to  $-70.56^\circ$ , whereas according to the minimum strain energy density theory, it is close to  $-83.62^\circ$ .

2.2 Experimental results on RT-PMMA

In addition to recalling some salient results obtained on the RT-PMMA of interest and detailed in Mat Jali and Longère (2020), this section gives the data that will be used later in the calibration and verification of the numerical modelling.

2.2.1 KW impact tests

A series of KW impact tests using a 40-mm inner diameter gas gun have been carried out on three different grades of commercial shock-resistant RT-PMMA, viz. Plexiglass Resist®, in the aim of investigating their absolute and relative crack arrest capability, see Mat Jali and Longère (2020a, b). The grades are RT-PMMA45, 65 and 100, with the increasing number corresponding to increasing rubber nanoparticle concentration and resulting impact toughness. The 40 mm-width, 82 mm-height and 6 mm-thickness KW-type specimens made of RT-PMMA were cut from extruded plates. The 20 mm-length and 300 μm-gap blunt notches were machined in the plates using a wire cutting machine. The 20 mm-diameter and 25 mm-length sub-calibrated projectiles made of hard steel were inserted in 40 mm-diameter and 80 mm-length polystyrene foam guides (or sabots) for a total mass of about 100 g. Impact velocities ranged from 20 to 100 m/s, with the values 20, 25, 30, 40, 50, 80, and 100 m/s. The KW-type specimen/projectile interaction and further crack

propagation were recorded using a high-speed camera at a rate of 100kfps and with a  $320 \times 192\text{pixel}^2$  spatial resolution.

During the impact test above 40 m/s, whatever the RT-PMMA grade, specimens are subjected to multi-fragmentation with the size and number of fragments depending on the grade. The number of fragments is increasing as the impact velocity is increasing from 50 to 80 m/s. At high impact velocity, specimens are completely shattered. A stress whitening zone forms at the notch and further to the crack tip and lips, acting as a retardant and even inhibitor to slow down if not prevent the crack propagation. A semi elliptical stress whitening region was also observed at the rear edge of specimens.

Due to their low rubber nanoparticle concentrations, no crack arrest was observed for RT-PMMA45 and RT-PMMA65 at the lowest impact velocities—once the crack initiates, it propagates throughout the whole specimen or/and branches to form a more or less complex crack pattern. In contrast, crack is seen to arrest inside the RT-PMMA100 specimens for impact velocities lower than 40 m/s, see Fig. 1. As the present study focuses on the crack arrest, only the relevant results for RT-PMMA100 at impact velocities lower than the critical impact velocity (defined as the impact velocity at crack arrest, viz. 40 m/s) are presented here while details of results for higher velocities can be found in Mat Jali and Longère (2020a, b).

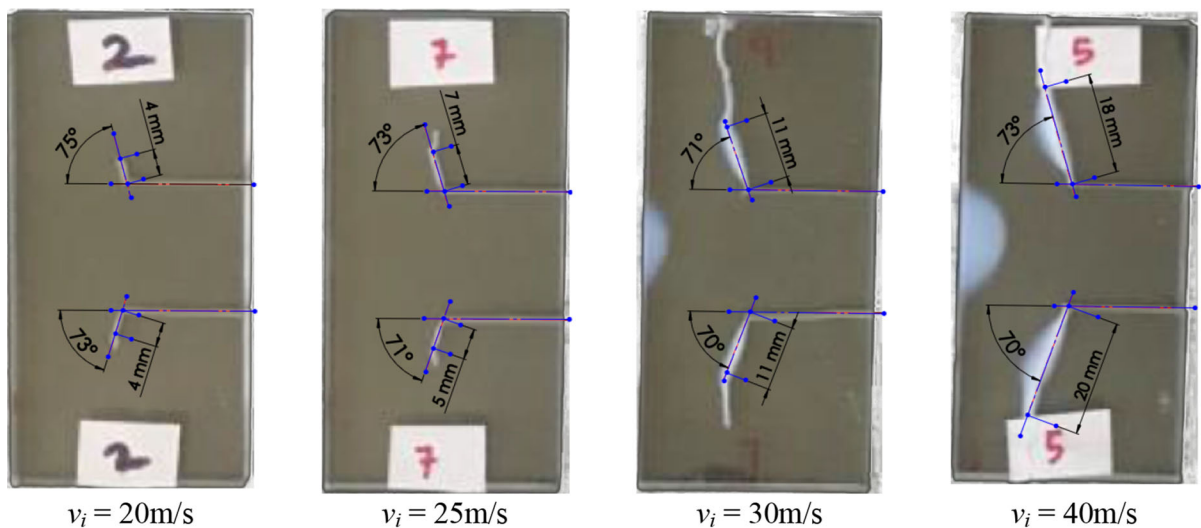


**Fig. 1** Experimental results for impact tests on RT-PMMA 100. Crack path in post-mortem specimens as a function of the impact velocity. Evidence of two cracks: a main (or primary) crack

initiated from the notch tip and a secondary crack initiated from the main crack tip. Length and orientation of the main crack are indicated on the pictures

Figure 1 evidences the presence of a main (or primary) crack initiated from the notch tip and oriented with an angle close to  $-72^\circ$  with respect to the notch plane and a secondary crack initiated from the main crack tip and oriented with an average angle close to  $-90^\circ$  with respect to the notch plane. The experimental main crack kink angle ( $\sim -72^\circ$ ) is slightly underestimated by the maximum hoop stress theory ( $-70.56^\circ$ ) and largely overestimated by the minimum strain energy density theory ( $-83.62^\circ$ ) when applied to pure Mode II shear loading, see subsection 2.1. The secondary crack path is tortuous and quasi orthogonal to the notch plane. The extension of the main crack is plotted against impact velocity in Fig. 2. Assuming coarsely a linear correlation, the extrapolated line intersects the abscissa at 16 m/s, which represents an estimate of the threshold impact velocity  $V_T$  causing crack initiation.

### 2.2.2 Thermomechanical characterization

The true stress-true plastic strain curves obtained from tension and compression loading at various low and high strain rates at room temperature are plotted in Fig. 3. According to the latter, the curve shows a peak followed by a strain softening and then a slight strain hardening. In addition, as for most glassy polymers, see e.g. Chou et al. (1973), Arruda et al. (1995) and Nasraoui et al. (2012), the material exhibits

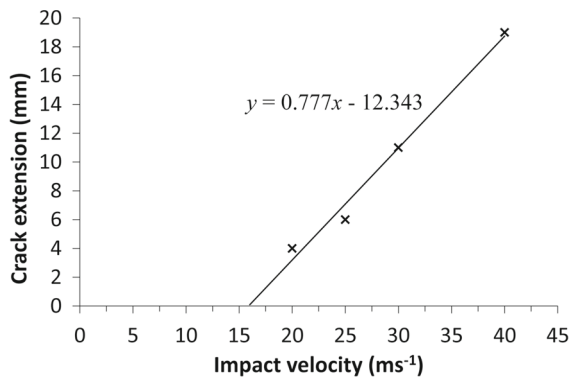


**Fig. 2** Experimental results for impact tests on RT-PMMA 100. Main crack length plotted against impact velocity. The dots correspond to the experimental data (see Fig. 1) and the straight line to a linear approximation. The threshold impact velocity  $V_7$  is estimated at about 16 m/s by extrapolating the straight line at 0 crack length

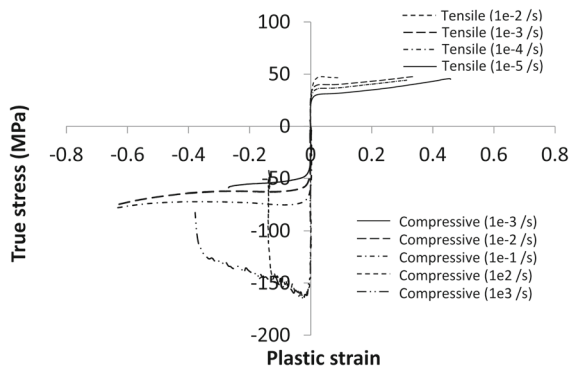


**Fig. 3** Experimental stress–strain curves of RT-PMMA 100. Strain rate effect. Room temperature

tension/compression asymmetry, strain-rate dependence and self-heating induced thermal softening at moderate to high strain rate. These effects must be accounted for in the numerical simulation.

### 3 Numerical procedure

The KW impact test initial and boundary value problem is set and solved employing the three-dimensional commercial computation code LS-DYNA R11.0 package using the explicit time integration scheme.

#### 3.1 Spatial discretization

The three-dimensional KW impact configuration considered herein, see Fig. 4, includes the doubly-notched plate made of RT-PMMA100, the sub-calibrated projectile made of hard steel and the projectile guide (sabot) made of low density foam. Due to the plate/projectile mechanical impedance mismatch, the plate is actually submitted to a multi-step loading of decreasing magnitude. Reproducing as correctly as possible this multi-step loading requires modelling the projectile and its sabot. In order to save computational time, the spatial discretization takes advantage of the symmetry of the different parts forming the KW impact set-up by modelling only the upper half. Symmetric boundary conditions are accordingly imposed. The doubly-notched plate and the projectile are modelled using particles (according to smooth particle hydrodynamics method, SPH) whereas the sabot is meshed using finite element (according to finite element method, FEM).

The minimum spacing between particles is dictated by the notch gap (the gap between the notch lips), for any lower spacing would fill up the gap in question. To keep a reasonable computation time, avoid unrealistic wave rebound at the interface between zones with potentially different particle densities and get a critical-maximum-principal-stress-to-static-yield-stress-ratio within the [2;3] range—as widely encountered in literature, see e.g. Batra and Gummalla, (2000), Batra and Ravinsankar, (2000), Li et al., (2002), and in Sects. 4 and 5 below, the particles are uniformly spaced at 300  $\mu\text{m}$ , except for the two rows forming the gap lips which need a slightly larger spacing to account for the particle volume and ensure the correct notch gap value. The plate was discretised into 20 equal layers along its thickness. The plate and the projectile three-dimensional models are discretised using 356,400 and 144,312 particles, respectively, see Fig. 4.

#### 3.2 Material description

We introduce the 2nd and 3rd invariants of the deviator  $\underline{s}$  of the Cauchy stress tensor  $\underline{\sigma}$ , namely  $J_2$  and  $J_3$ , as

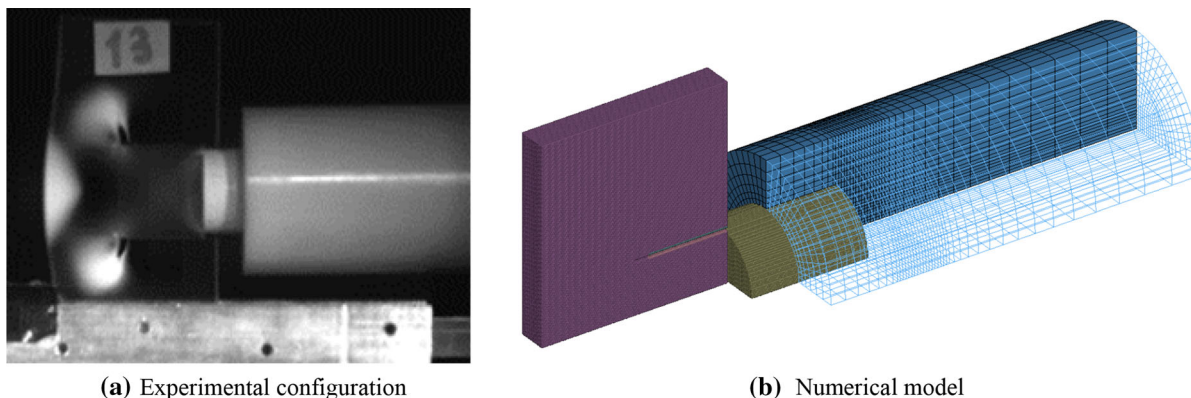


**Fig. 4** Experimental configuration and numerical model of KW impact test. In the model, the plate and the projectile are modelled with particles (SPH) and the sabot with meshes (FEM)

$$J_2 = \frac{1}{2} \underline{\underline{s}} : \underline{\underline{s}} ; J_3 = \det \underline{\underline{s}} ; \underline{\underline{s}} = \underline{\underline{\sigma}} - \frac{\text{Tr} \underline{\underline{\sigma}}}{3} \underline{\underline{I}} \quad (17)$$

where det stands for determinant and Tr for trace. The equivalent stress  $\sigma_{eq}$  and Lode parameter  $L$  may accordingly be written as

$$\sigma_{eq} = \sqrt{3J_2} ; L = \cos(3\theta_L) = \frac{27J_3}{2\sigma_{eq}^3} \quad (18)$$

where  $\theta_L$  is the Lode angle. It is noteworthy that  $L = -1$  in compression,  $L = +1$  in tension and  $L = 0$  in shear.

According to the  $J_2$  viscoplastic flow theory, the yield function reads

$$\begin{aligned} f(\underline{\underline{\sigma}}, \sigma_y) &= f(J_2(\underline{\underline{\sigma}}), \sigma_y) \\ &= \sigma_{eq}(J_2(\underline{\underline{\sigma}})) - \sigma_y(T, \varepsilon_{eq}^p, \dots) \\ &= \sigma_v(T, \varepsilon_{eq}^p, \dot{\varepsilon}_{eq}^p, \dots) \geq 0 \end{aligned} \quad (19)$$

where  $\sigma_y$  and  $\sigma_v$  are respectively the rate independent and viscous stresses,  $T$  the temperature,  $\varepsilon_{eq}^p$  and  $\dot{\varepsilon}_{eq}^p$  the equivalent (or cumulated) plastic, strain and strain rate. ... inside the brackets means that other variables can be accounted for (damage f.ex.). Equation (19) yields

$$\begin{aligned} \sigma_{eq}(J_2(\underline{\underline{\sigma}})) &= \bar{\sigma}_y(T, \varepsilon_{eq}^p, \dot{\varepsilon}_{eq}^p, \dots) ; \bar{\sigma}_y(T, \varepsilon_{eq}^p, \dot{\varepsilon}_{eq}^p, \dots) \\ &= \sigma_y(T, \varepsilon_{eq}^p, \dots) + \sigma_v(T, \varepsilon_{eq}^p, \dot{\varepsilon}_{eq}^p, \dots) \end{aligned} \quad (20)$$

with  $\bar{\sigma}_y$  the rate dependent yield stress. A way of accounting for the 3<sup>rd</sup> invariant  $J_3$  to reproduce e.g.

strength asymmetry may be to write the yield function in the form

$$\begin{aligned} \hat{f}(\underline{\underline{\sigma}}, \sigma_y) &= \hat{f}(J_2(\underline{\underline{\sigma}}), J_3(\underline{\underline{\sigma}}), \sigma_y) \\ &= \hat{\sigma}_{eq}(J_2(\underline{\underline{\sigma}}), J_3(\underline{\underline{\sigma}})) - \sigma_y(T, \varepsilon_{eq}^p) \\ &= \sigma_v(T, \varepsilon_{eq}^p, \dot{\varepsilon}_{eq}^p) \geq 0 \end{aligned} \quad (21)$$

where  $\hat{\sigma}_{eq}$  is a transformed equivalent stress. Equation (21) yields

$$\begin{aligned} \hat{\sigma}_{eq}(J_2(\underline{\underline{\sigma}}), J_3(\underline{\underline{\sigma}})) &= \bar{\sigma}_y(T, \varepsilon_{eq}^p, \dot{\varepsilon}_{eq}^p) ; \bar{\sigma}_y(T, \varepsilon_{eq}^p, \dot{\varepsilon}_{eq}^p) \\ &= \sigma_y(T, \varepsilon_{eq}^p) + \sigma_v(T, \varepsilon_{eq}^p, \dot{\varepsilon}_{eq}^p) \end{aligned} \quad (22)$$

In the sequel, two plasticity models will be used.

- $J_2$  plastic flow theory-related model with plastic strain dependence,
- $J_3$ -dependent (so-called-in-LS-DYNA) generalized yield stress (GYS) model with plastic strain, plastic strain rate and temperature dependence.

High strength steels are generally only weakly rate dependent. In addition, if the plastic strain remains small, self-heating can be neglected and then accounting for temperature is not necessary. According to the  $J_2$  plastic flow theory with plastic strain dependence, the yield function in (19) and the equivalent stress in (20) reduce to

$$\begin{aligned}
 f(\underline{\sigma}, \sigma_y) &= f(J_2(\underline{\sigma}), \sigma_y) = \sigma_{eq}(J_2(\underline{\sigma})) - \sigma_y(\dot{\epsilon}_{eq}^p) \\
 &= 0; \quad \sigma_{eq}(J_2(\underline{\sigma})) = \sigma_y(\dot{\epsilon}_{eq}^p)
 \end{aligned}
 \tag{23}$$

Even in absence of initial material symmetry, most glassy polymers exhibit tension/compression asymmetry. This strength asymmetry in polymers is often accounted for in constitutive models via a  $I_1$ -dependence, where  $I_1$  is the 1st invariant of the stress tensor (related to the opposite of the pressure), see e.g. Aruda and Boyce (1995) for PMMA. It can also be accounted for via a  $J_3$ -dependence, as does the GYS model implemented in LS-DYNA, that allows precisely for reproducing strength asymmetry in tension, compression and shear of isotropic materials. According to the GYS model, the transformed equivalent stress takes the form

$$\begin{aligned}
 \hat{\sigma}_{eq}(J_2(\underline{\sigma}), J_3(\underline{\sigma})) &= \sigma_{eq}(J_2(\underline{\sigma})) \times \\
 &\left( c_1 + c_2 L(J_2(\underline{\sigma}), J_3(\underline{\sigma})) + c_3 L^2(J_2(\underline{\sigma}), J_3(\underline{\sigma})) \right)
 \end{aligned}
 \tag{24}$$

Knowing the yield stress in tension  $\sigma_T$ , in compression  $\sigma_C$  and in shear  $\sqrt{3}\sigma_S$ , the rate dependent yield stress  $\bar{\sigma}_y$ , and coefficients  $c_1$ ,  $c_2$  and  $c_3$  in (24) are determined by

$$\begin{aligned}
 \bar{\sigma}_y(T, \dot{\epsilon}_{eq}^p, \dot{\epsilon}_{eq}^p) &= \sigma_T(T, \dot{\epsilon}_{eq}^p, \dot{\epsilon}_{eq}^p); \quad c_1(T, \dot{\epsilon}_{eq}^p, \dot{\epsilon}_{eq}^p) = \frac{\sigma_T(T, \dot{\epsilon}_{eq}^p, \dot{\epsilon}_{eq}^p)}{\sqrt{3}\sigma_S(T, \dot{\epsilon}_{eq}^p, \dot{\epsilon}_{eq}^p)}; \\
 c_2(T, \dot{\epsilon}_{eq}^p, \dot{\epsilon}_{eq}^p) &= \frac{1}{2} \left( 1 - \frac{\sigma_T(T, \dot{\epsilon}_{eq}^p, \dot{\epsilon}_{eq}^p)}{\sigma_C(T, \dot{\epsilon}_{eq}^p, \dot{\epsilon}_{eq}^p)} \right); \quad c_3(T, \dot{\epsilon}_{eq}^p, \dot{\epsilon}_{eq}^p) = 1 - \left( c_1(T, \dot{\epsilon}_{eq}^p, \dot{\epsilon}_{eq}^p) + c_2(T, \dot{\epsilon}_{eq}^p, \dot{\epsilon}_{eq}^p) \right)
 \end{aligned}
 \tag{25}$$

Coefficients  $c_1$ ,  $c_2$  and  $c_3$  are thus potentially plastic strain, plastic strain rate and temperature dependent. If now  $\sigma_C = \sigma_T$  and  $\sigma_S = \frac{\sigma_T}{\sqrt{3}}$  then  $c_1 = 1$ ,  $c_2 = c_3 = 0$ , yielding  $\hat{\sigma}_{eq}(J_2(\underline{\sigma}), J_3(\underline{\sigma})) = \sigma_{eq}(J_2(\underline{\sigma}))$ , and the  $J_2$  flow theory is retrieved.

Inelastic dissipation induced temperature rise under adiabatic condition is estimated according to

$$T - T_R = \frac{\beta}{\rho C_p} \int \sigma_y d\dot{\epsilon}_{eq}^p
 \tag{26}$$

where  $T_R$  is the initial (room) temperature,  $\rho$  and  $C_p$  the mass density and specific heat, and  $\beta$  the inelastic heat fraction (proportion of inelastic work rate converted into heat) also known as Taylor-Quinney coefficient. The inelastic heat fraction  $\beta$  has been seen to notably depend on strain, see e.g. Rittel (1999) for polycarbonate. Yet, a reliable expression for  $\beta$  is still missing and an arbitrary constant value is generally assumed, see e.g. Pan et al. (2016) for epoxy resin or Bjerke et al. (2002) for polycarbonate.

Physical and elastic properties of the three parts forming the KW-impact test set-up are reported in Table 1.

For KW doubly-notched plates made of initially isotropic RT-PMMA, the strain-, rate-, temperature- and loading sign-dependence of the material behaviour was reproduced using the GYS model available in LS-DYNA (MAT\_224\_GYS), see Eqs.(21, 22), (24–25). Tensile  $\sigma_T$  and compressive  $\sigma_C$  yield stresses in Eq. (25) were provided in the form of tabulated stress–strain curves at various strain rates and temperatures, see Fig. 5—while shear  $\sigma_S$  yield stress was assumed to satisfy  $J_2$ -flow theory – allowing the determination of the rate dependent yield stress  $\bar{\sigma}_y$ , and coefficients  $c_1$ ,  $c_2$  and  $c_3$  in Eq. (25). The stress–strain

curves in question include the experimental ones, see Fig. 3, completed by extrapolated responses for high strain rate loading, in particular in tension for which no high strain rate experimental results were available, and high temperature. In absence of further information for the RT-PMMA under consideration, self-heating at high strain rate is estimated considering that 100% of the plastic work rate are converted into heat

**Table 1** Physical and elastic properties for the model

	Plate specimen (RT-PMMA 100)	Projectile (High strength steel)	Sabot (Foam)
Density $\rho$ (kg/m <sup>3</sup> )	1170	7850	335
Young's modulus $E$ (MPa)	1525	$2.05 \times 10^5$	250
Poisson's ratio $\nu$	0.38	0.28	–
Specific heat $C_p$ (J/kg/K)	1466	420	1215
Thermal conductivity $k$ (W/m K)	0.2	50.2	0.1

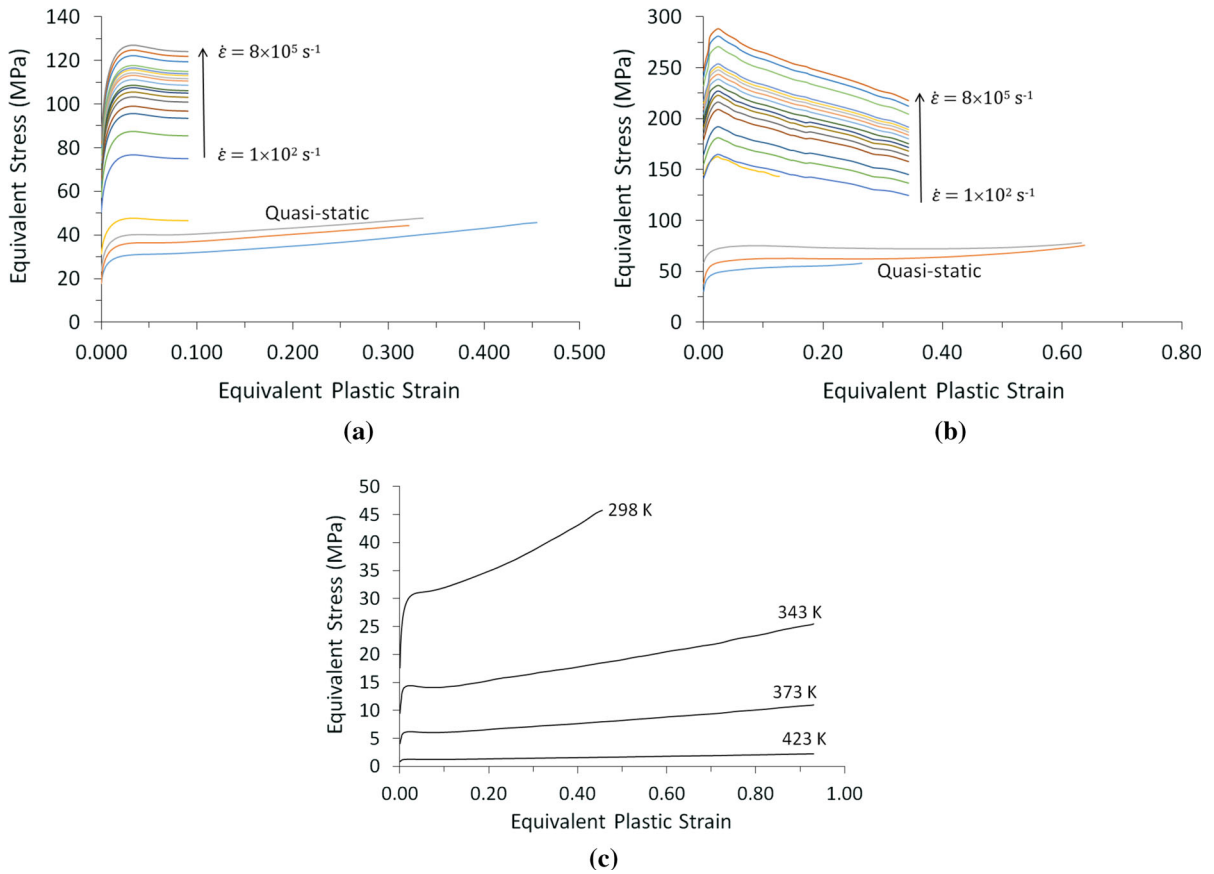


**Fig. 5** Input data in terms of stress–strain curves: **a** tensile stress at various strain rates; **b** compressive stress at various strain rates; **c** tensile stress at various temperatures

[inelastic heat fraction  $\beta = 1$  in Eq. (26)], as implicitly done in Estevez and Basu (2008) for plain PMMA.

Though the Young’s modulus of the projectile is much higher than the plate’s one, see Table 1, the projectile was not modelled by a rigid body but by an elasto-plastic material with piecewise linear plasticity (MAT\_024 in LS-DYNA) using the tabulated stress–strain curve in Fig. 6a in order to reproduce the physical stress wave propagation and interaction. In a same way, to preserve the real mass and further kinetic

energy involved at the impact instant, the sabot was also included in the model as low density foam (MAT\_057 in LS-DYNA) with a tabulated stress–strain curve, see Fig. 6b.

### 3.3 SPH formulation and contact conditions

Though setting up the SPH simulation model is rather straightforward, there are two crucial aspects to be taken care of in order to successfully produce a robust

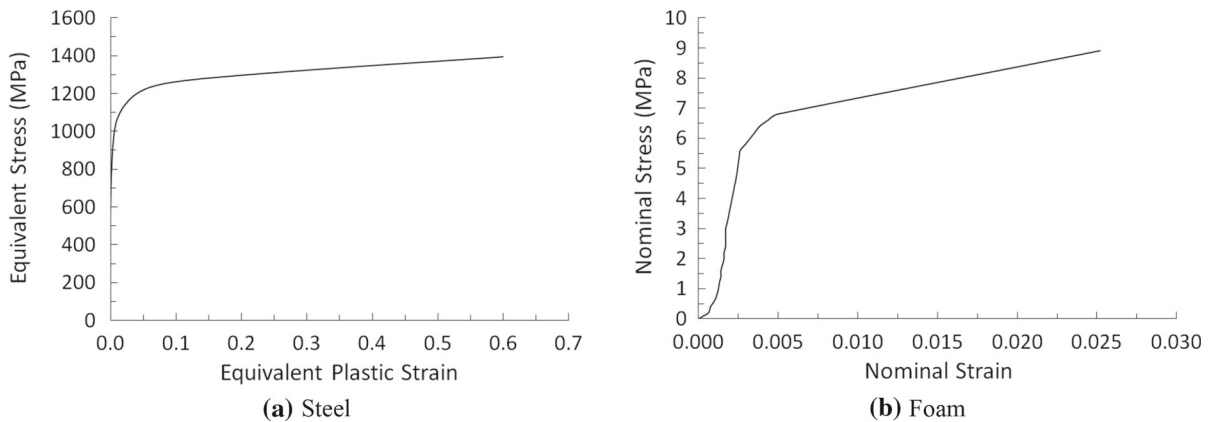


**Fig. 6** Stress–strain curves used to describe the behaviour of the steel (projectile) and the polyethylene foam (sabot)

model, namely the SPH theory approximation and the contact condition.

### 3.3.1 SPH formulation

Numerous SPH theory approximations are available in LS-DYNA. Formulations based on Lagrangian or Eulerian kernel are recommended to alleviate the well-known SPH pathological issue related to tensile instability, see e.g. Yreux (2018). Lagrangian formulation is limited to moderate deformation whereas Eulerian formulation can be used for very large deformation while being very time consuming. In the present application, viz. fracture of RT-PMMA under impact loading, the material undergoes small to moderate deformation before failure. The total Lagrangian formulation with renormalization (FORM#8 in LS-DYNA) is accordingly adopted.

### 3.3.2 Contact conditions

Preventing penetration is of utmost importance regarding the transferred momentum and resulting degradation. In the present case, the main issue regarding penetration is twofold, as illustrated in Fig. 7: between the projectile and the plate on the one hand, and between the notch lips on the other hand. In LS-DYNA, for SPH particles approximated using the total Lagrangian formulation the neighbouring lists are only updated at the beginning of the simulation. Consequently, the one suitable contact interaction method is the node-to-node penalty based contact. This implies that inter-part interaction be not performed using particle approximation but through a SPH-to-SPH coupling. On the other hand, the penetration was found to be decreasing with decreasing time step. For example, a time scale factor of 0.2 is

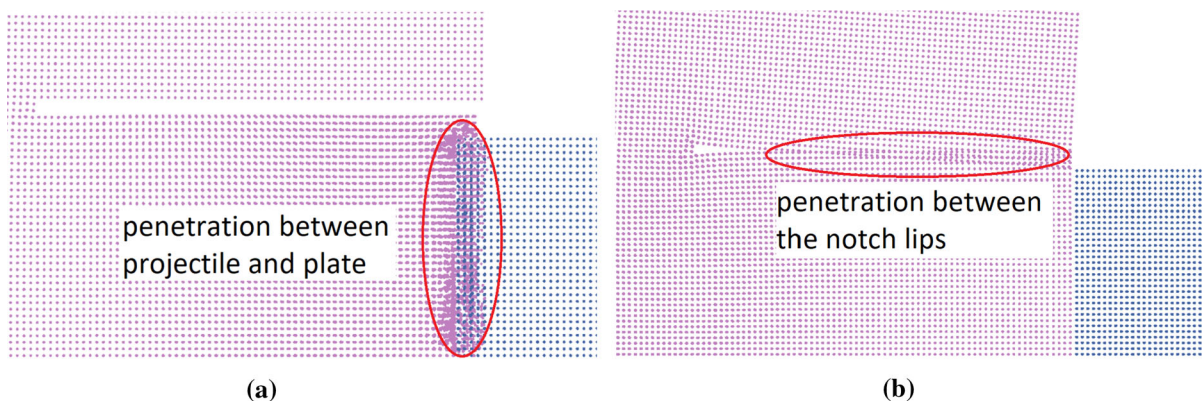


**Fig. 7** Consequences of improper contact definitions: **a** penetration between the projectile and the plate, and **b** penetration between the plate notch lips

seen to be sufficient to minimize the penetration and attenuate numerical instability for moderate impact velocity (lower than 50 m/s in the present case), whereas a time scale factor of 0.1 and lower is needed for high impact velocity (greater than 50 m/s in the present case).

Yet, the above settings happened to be insufficient to fully prevent penetration. Indeed, the notches lips were seen to keep on severely penetrating each other, as shown in Fig. 7b. The approach adopted here to alleviate this issue was to define a single layer of each notch lip individually and then define the required contact between these two parts through SPH-to-SPH coupling as well. This is depicted in Fig. 8. The settings are similar to the one defined for the plate and the projectile.

### 3.4 Continuity of the velocity at the projectile/plate interface

The verification of the interface velocity is crucial to be sure that the predetermined impact load is effectively transferred from the projectile to the plate edge so that the predetermined loading condition is exerted as expected. Significant penetrations would indeed reduce the effectiveness of the load transmission.

According to a coarse approximation based on one-dimensional elastic wave propagation theory, one can estimate the material velocity at the projectile/plate interface  $V_S$  as a function of the initial impact velocity  $V_I$  as follows

$$\frac{V_S}{V_I} = \frac{1}{1 + \frac{Z_P}{Z_S}} \tag{27}$$

with

$$\begin{cases} Z_S = \sqrt{(\rho E)_S} \frac{\pi D^2}{4} \\ Z_P = \sqrt{(\rho E)_P} wh \end{cases} \tag{28}$$

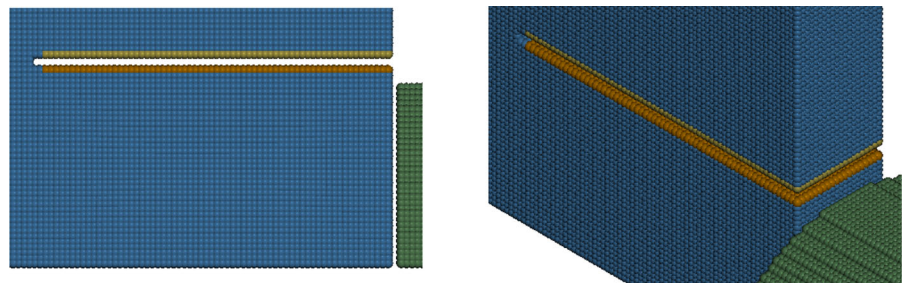
where  $Z_S$  and  $Z_P$  represent the mechanical impedances of the projectile (striker) and the plate,  $w$  and  $h$  the thickness and height of the impacted part of the plate and  $D$  the projectile diameter. After injecting into (27–28) the dimensions of the plate and projectile given in subsection 2.2.1 and the elastic properties in Table 1, the ratio  $V_S/V_I$  is close to 98.6%. Similarly, the time period of the wave train related to the projectile,  $T_S = 2L_S/C_S$ , with  $L_S$  and  $C_S$  the projectile length and wave speed, is close to 10  $\mu$ s.

The average numerical material velocity over the 760 particles on the contact surface between the plate and the projectile is depicted in Fig. 9. It can be seen that the particles on the contact surface achieved about 98% of initial impact velocity, as expected. In addition, a perfect projectile/plate impedance match would induce a velocity drop at 10  $\mu$ s, whereas a projectile/plate impedance mismatch induces a multi-step loading with a decreasing magnitude at the projectile time period of 10  $\mu$ s, as visible in the velocity history in Fig. 9.

## 4 Preliminary numerical analysis

In this section, after conducting a numerical stress analysis near the notch tip, we examine the ability of some failure criteria to reproduce qualitatively the experimental results summarised in subsection 2.2.1. According to the linear approximation considered in subsection 2.2.1, see Fig. 2, the threshold impact velocity  $V_T$ , or impact velocity at crack initiation, is close to 16 m/s. A pertinent failure criterion is

**Fig. 8** Approach adopted to neutralise the penetration between the notch lips



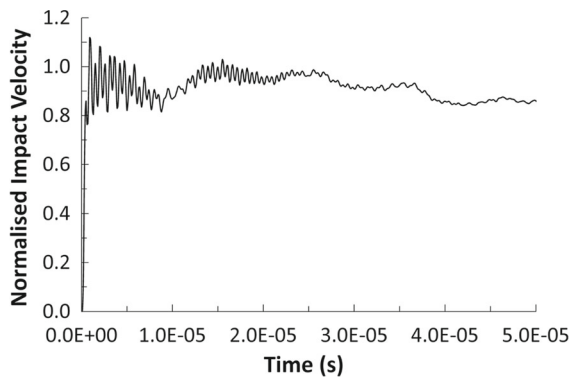
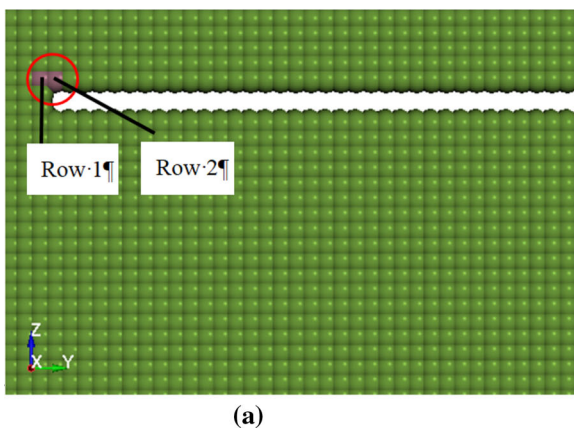


**Fig. 9** Evolution of the normalised impact velocity on the contact surface of the plate edge

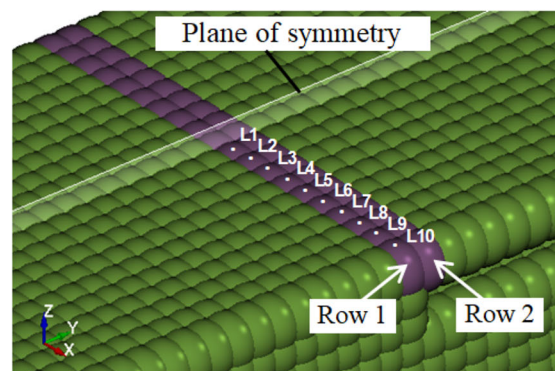
accordingly expected to lead to crack formation only for impact velocities greater than this value.

#### 4.1 Numerical stress analysis

To obtain some insights on how stress levels at the notch tip evolve along the impact loading, a preliminary numerical stress analysis was first conducted without imposing any failure criteria. The region of interest is the upper corner of the notch tip, where the crack typically initiated in the experimental tests, see Fig. 10a. Figure 10b depicts the selected two rows of the particles across the thickness of the plate, viz. row 1 and row 2. Since the loading is symmetric with respect to the midplane along the thickness of the



(a)



(b)

**Fig. 10** Definition of the groups of particles. **a** Side view of layer L10; **b** inclined view. Each layer covers all the particles located inside a plane parallel to the plate side and layers are numbered from the plate center (L1) towards the plate (free) side

plate, only the stress and strain analysis of the front half plate will be considered.

Time histories of the maximum principal stress (MPS) for impact at  $V_I = 16$  m/s for the particles in rows 1 and 2 are plotted in Fig. 11a and b, respectively. The stress level is generally slightly higher in row 1 than in row 2. On the other hand, when moving across the thickness of the plate, from the plate center towards the plate free surface, MPS magnitude is seen to slightly decrease. If the failure criterion is expressed in terms of critical MPS (CMPS), that means that the failure will first initiate in particles located near the plate center in either row 1 or row 2. Among the curves, there are three curves of dashed-line type that are visibly lower than the others and corresponding to the three outermost particles on each side of the free surface of the plate along the thickness of the plate. Since the particles with highest stress level will reach the failure criteria and spark the failure first, the three outer particles were excluded in the subsequent analysis, and focus will be on particles at the intersection between rows 1–2 and layers L1–L7. Special attention will be given to the layers that experience the maximum stress level as the latter dictates whether the crack will initiate, which generally is in the mid-layer, or L1.

Simulations were also conducted for  $V_I = 18$  and 20 m/s and the MPS were found to follow similar evolution while reaching higher stress level, as expected. From the MPS time histories of  $V_I = 16$  m/s, the maximum value of MPS achieved is

(L10). A row is a line of particles crossing the thickness of the plate and containing 2 particles (one on each end) located on the plate (free) side

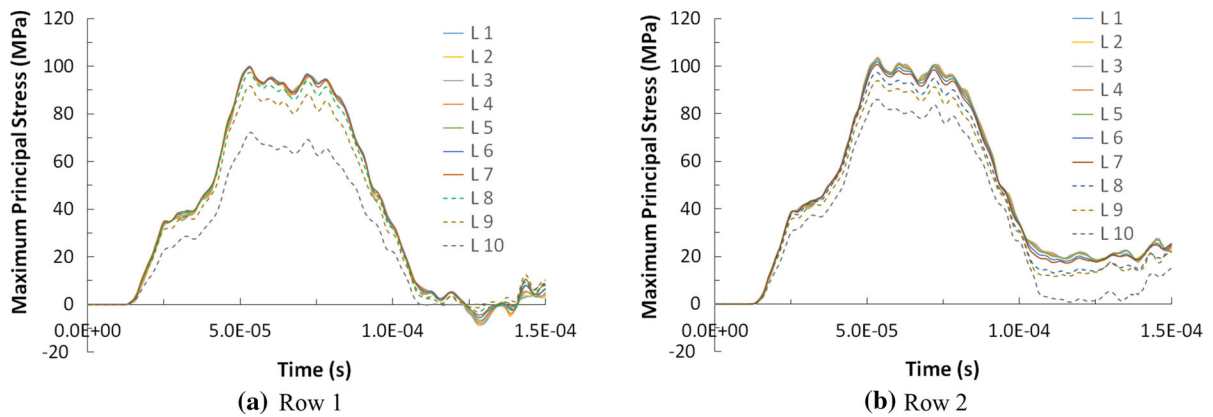


**Fig. 11** Numerical simulation considering an impact at 16 m/s. No failure criterion. Evolution of maximum principal stress (MPS) at the notch tip for particles belonging to **a** row 1; **b** row 2, see also Fig. 10

104 MPa. Thus the reasonable prediction for the critical MPS (CMPS) shall be slightly lower so that when such failure criteria is applied, the crack will be initiated at  $V_I = 16$  m/s. In addition, according to (7), the critical stress intensity factor  $K_{I_c}$  reads

$$K_{I_c} = \sqrt{\pi a} \sigma_c \quad (19)$$

By coarsely associating the CMPS with the critical stress  $\sigma_c$ , and accounting for the notch length, this would lead to  $K_{I_c} = 26 \text{MPa} \cdot \sqrt{m}$  at crack initiation for the RT-PMMA under consideration, viz. RT-PMMA100. It is noteworthy that this value would be more than 10 times values of quasi-static  $K_{I_c}$  ( $K_{I_c} \approx 2 \text{MPa} \cdot \sqrt{m}$ ) and 6 times values of dynamic  $K_{I_c}$  ( $K_{I_c} \approx 4 \text{MPa} \cdot \sqrt{m}$ ) available in literature for unmodified PMMA, see e.g. Lalande et al. (2006) and Weerasooriya et al. (2006). This numerical value for  $K_{I_c}$  at crack initiation is clearly widely overestimated. This will be confirmed in the following section. However, this value of 104 MPa as potential critical MPS equals 2.6 times the static yield stress of 40 MPa (average value over the 3 quasi static curves in Fig. 5a), and is then within the [2;3] range as expected.

## 4.2 Identification of failure criteria

When dealing with brittle fracture, the failure criterion is generally expressed in terms of critical stress (which is related to the critical stress intensity factor), see, for example, Raymond et al. (2014), whereas for ductile failure it is generally expressed in terms of critical strain (to account for the material ductility), see, for

example, Zhou et al. (1996b). In the present case, the brittle nature of the PMMA matrix would lead to adopt a critical stress-controlled failure criterion, but the rubber nanoparticles inside the PMMA matrix have been seen to induce a form of ductility which would accordingly lead to adopt a critical strain-controlled failure criterion.

Considering that the RT-PMMA exhibits a semi-brittle/semi-ductile behaviour, it was thus decided to investigate both stress- and strain-controlled failure criteria, first individually and then in a combined way. For that purpose, numerical parametric studies were performed to reproduce the fracture conditions at various impact velocities as observed during the experimental tests. For each impact configuration, the numerical maximum principal stress and plastic strain distribution in the specimen and their evolution at the critical point of the crack tip, i.e. the particles along rows 1 and 2, were analysed.

### 4.2.1 Critical maximum principal stress (CMPS) as failure criterion

Based on the initial estimation of the CMPS in subsection 4.1, simulations were performed with a CMPS of 103 MPa. The outcomes are presented in Fig. 12 for several increasing impact velocities starting from the threshold impact velocity  $V_T$ . In addition, the influence of impact velocity in terms of MPS evolution is shown in Fig. 13.

According to Fig. 12, the crack initiates at the notch tip as expected. However, it unexpectedly does not arrest inside the specimen but propagates throughout

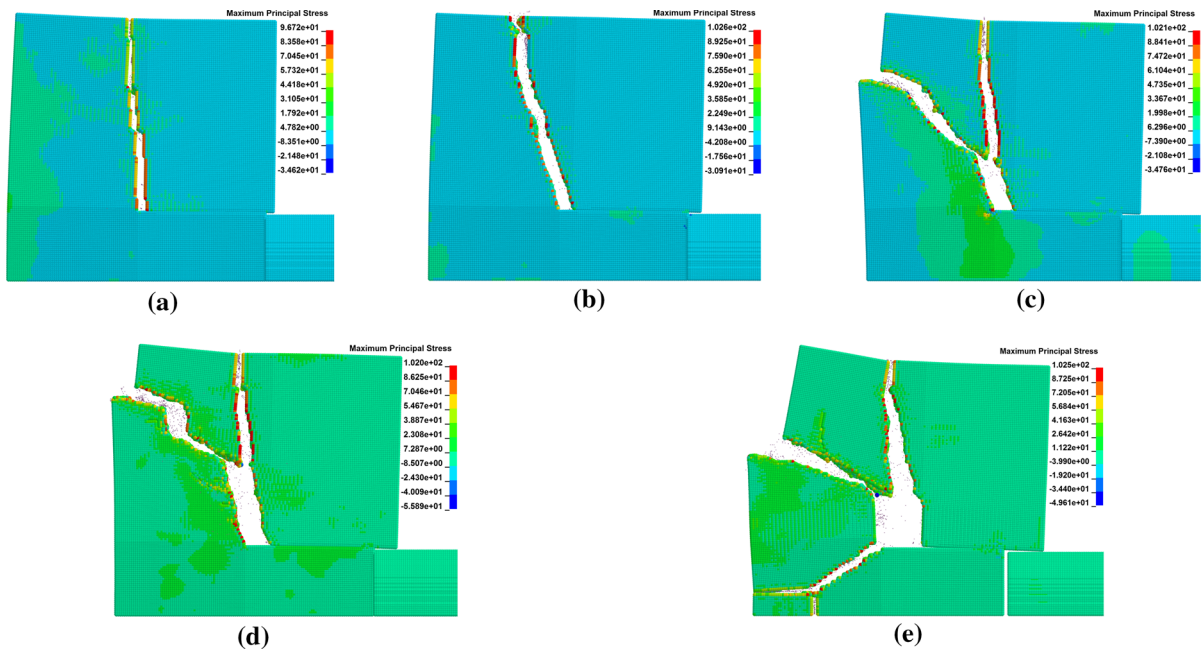


**Fig. 12** Numerical simulation for the CMPS of 103 MPa. MPS isocontours for **a**  $v_i = 16$  m/s; **b** 20 m/s; **c** 25 m/s; **d** 30 m/s; **e** 40 m/s

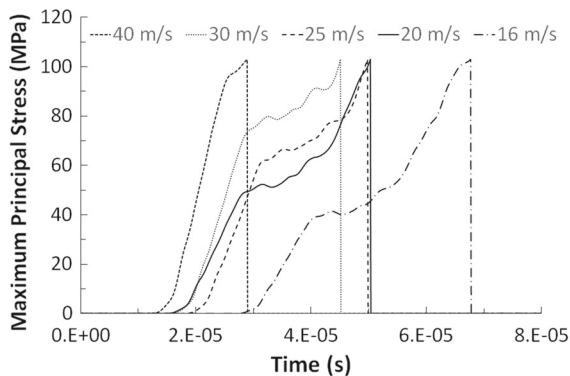


**Fig. 13** Numerical MPS time history in particle 1 of row 2 for various impact velocities. Critical MPS of 103 MPa

the whole specimen even at the threshold impact velocity  $V_7$ . At 25 and 30 m/s, the crack is seen to be branching and at 40 m/s another crack initiates from the notch tip and propagates towards the rear edge of the specimen. On the other hand, the main crack kink angle absolute value is greater than  $72^\circ$  (which is the value experimentally measured). This suggests that the used failure criterion and/or the value of the critical MPS, see Fig. 13, are inappropriate.

In view of investigating the influence of the CMPS on the failure conditions, several simulations were performed at a given impact velocity with different

values of CMPS around the threshold impact velocity value determined previously. CMPS values were 70, 80, 90, 110 and 120 MPa, and the impact velocity was 20 m/s. MPS isocontours in the specimen under impact loading are visible in Fig. 14, and MPS evolutions are plotted in Fig. 15. According to Fig. 14, whatever the CMPS, and even for the highest values, all the simulations fail to reproduce the crack arrest, and the crack propagated throughout the whole plate. Similarly, the main crack kink angle absolute value was seen to generally increase with increasing CMPS. Multi-fragmentation occurred at 70 MPa, i.e. for the lowest CMPS value. From the plot of stress time history in Fig. 15, it can be seen that the fracture occurs later in the elastoplastic regime for highest MPS values. This confirms that the previous estimate of  $K_{Ic}$  at crack initiation is not pertinent.

One can conclude that the sole CMPS-controlled failure criterion is not able to reproduce the crack arrest.

#### 4.2.2 Critical equivalent plastic strain (CEPS) as failure criterion

We now investigate the ability of a plastic failure strain (CEPS)-controlled failure criterion to reproduce

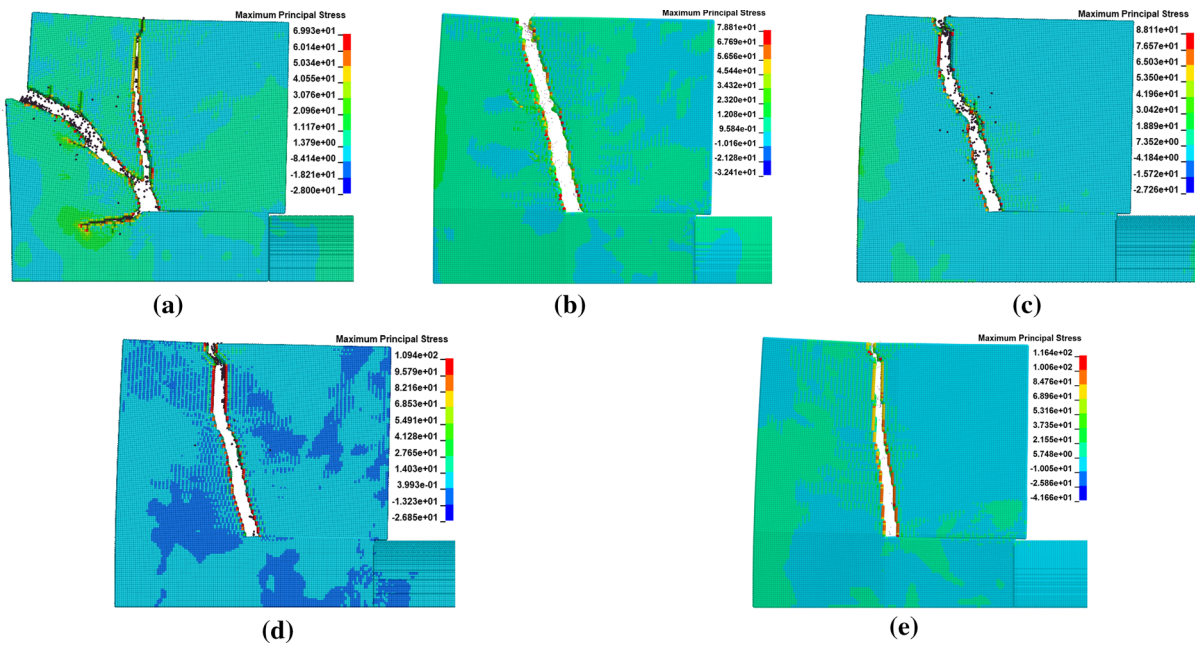


**Fig. 14** Numerical simulation for impact velocity of  $20 \text{ ms}^{-1}$  with different CMPS levels: **a** 70 MPa, **b** 80 MPa, **c** 90 MPa, **d** 110 MPa, **e** 120 MPa

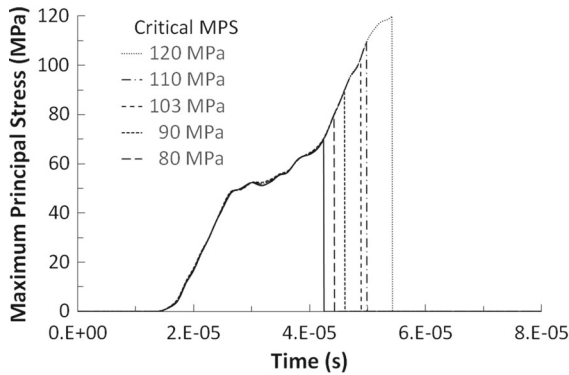


**Fig. 15** Numerical MPS time history in particle 1 of row 2 for various CMPS values. Impact velocity of 20 m/s

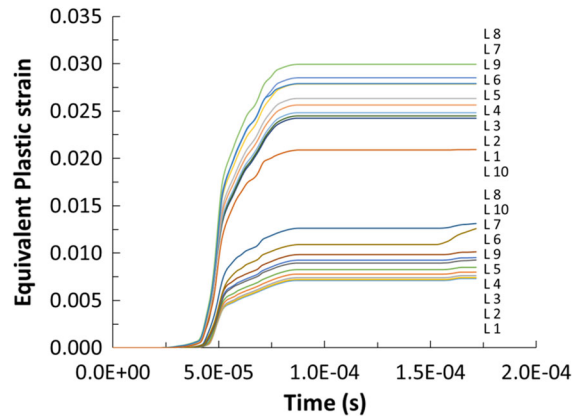


**Fig. 16** Numerical simulation considering an impact at 16 m/s. No failure criterion. Evolution of plastic strain at the notch tip for particles belonging to row 1 (lower curves) and row 2 (upper curves), see also Fig. 9

the fracture conditions experimentally observed. An approach similar as the one followed previously in subsection 4.1 is adopted. Indeed, from the numerical simulation conducted for impact velocity of 16 m/s and without any failure criteria, the equivalent plastic strain at the notch tip was extracted at the particles belonging to rows 1 and 2 in Fig. 10b and plotted in Fig. 16.

According to Fig. 16, the strain at the notch tip increases from the mid-layer towards the free surface of the plate, except for a few intermediate layers which

showed the lowest strain levels. The highest equivalent plastic strain achieved throughout the impact is seen to be  $2.99 \times 10^{-2}$ . Consequently, a slightly lower value, for example  $2.9 \times 10^{-2}$ , can be used as a first estimate of CEPS value producing a minimum yet observable crack initiation at the notch tip.

Numerical simulations were conducted using a CEPS of  $2.9 \times 10^{-2}$  with  $V_i = 16, 20, 25, 30$  and

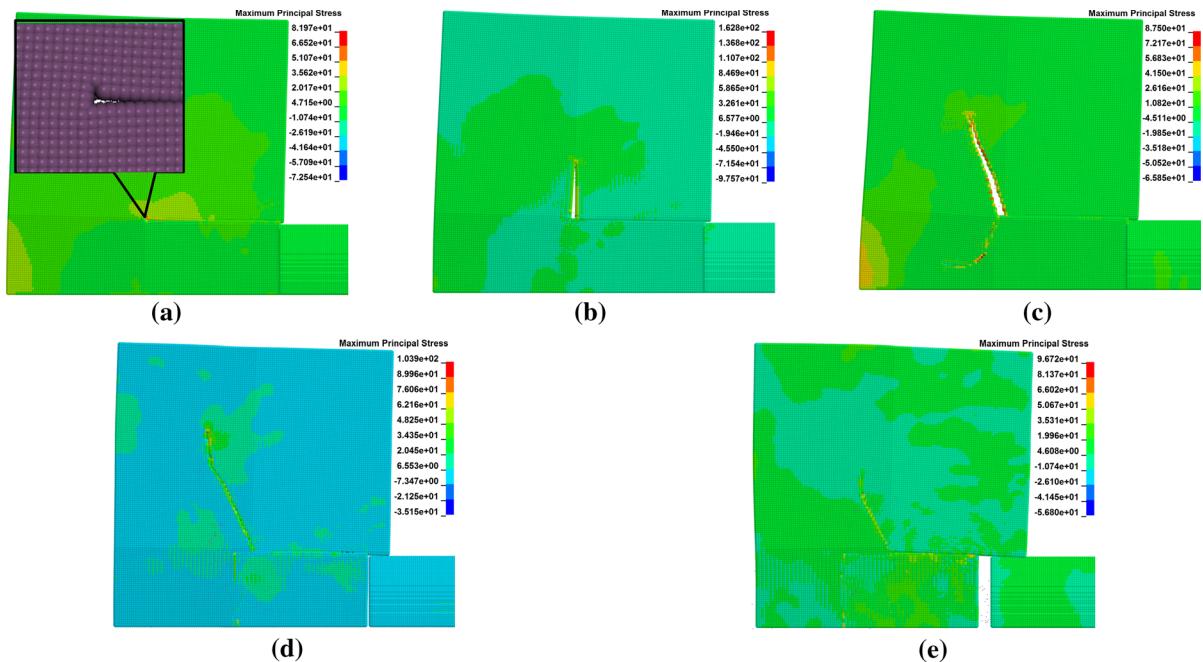


**Fig. 17** Numerical simulation for the CEPS of 0.029. MPS isocontours for  $V_I$  of **a** 16, **b** 20, **c** 25, **d** 30, and **e** 40 m/s

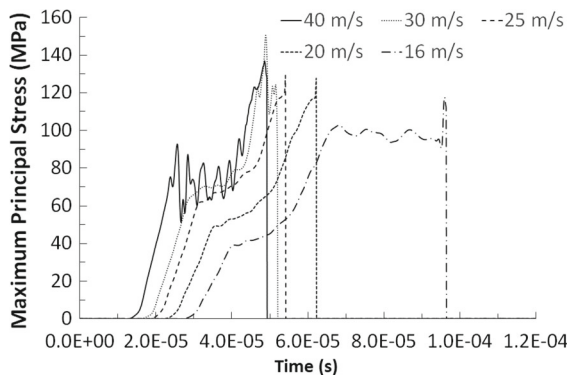


**Fig. 18** Numerical MPS time history in particle 1 of row 2 for various impact velocities. CEPS of  $2.9 \times 10^{-2}$

40 m/s. Corresponding results are presented in Fig. 17 in terms of isocontours and in Fig. 18 in terms of MPS evolution in a particle located at the notch tip. The CEPS-controlled failure criterion clearly managed to reproduce the crack arrest. Yet, the main crack kink angle absolute value seems to decrease with increasing impact velocity, starting at about  $90^\circ$  at 20 m/s and reaching about  $60^\circ$  at 40 m/s. On the other hand, another crack is seen to initiate from the notch tip and propagate downwards, which is not the case in the experiments.

Extra numerical simulations were also performed for CEPS values around  $2.9 \times 10^{-2}$  at the impact velocity of 20 m/s, see Fig. 19. Corresponding MPS time histories are plotted in Fig. 20. As expected the crack length is decreasing with increasing CEPS. It is noteworthy that the higher the CEPS the higher the kink angle absolute value.

One can thus conclude that the sole CEPS-controlled failure criterion is able to reproduce the crack arrest but reproduces the unintended propagation of another crack from the notch tip.

#### 4.2.3 Towards combined failure criteria

The above analysis demonstrated that none of the CMPS- and CEPS-dependent failure criteria is individually able to reproduce the crack initiation, arrest and pattern observed experimentally. In particular, based upon linear fracture mechanics theory the CMPS criterion is unable to reproduce the crack arrest, and if the CEPS criterion is sufficiently able to reproduce crack arrest it leads to the unrealistic formation of another crack. Preventing the latter seems to be the solution for reproducing the real picture. For this reason, we examine the ability of a combination of both CMPS and CEPS failure criteria

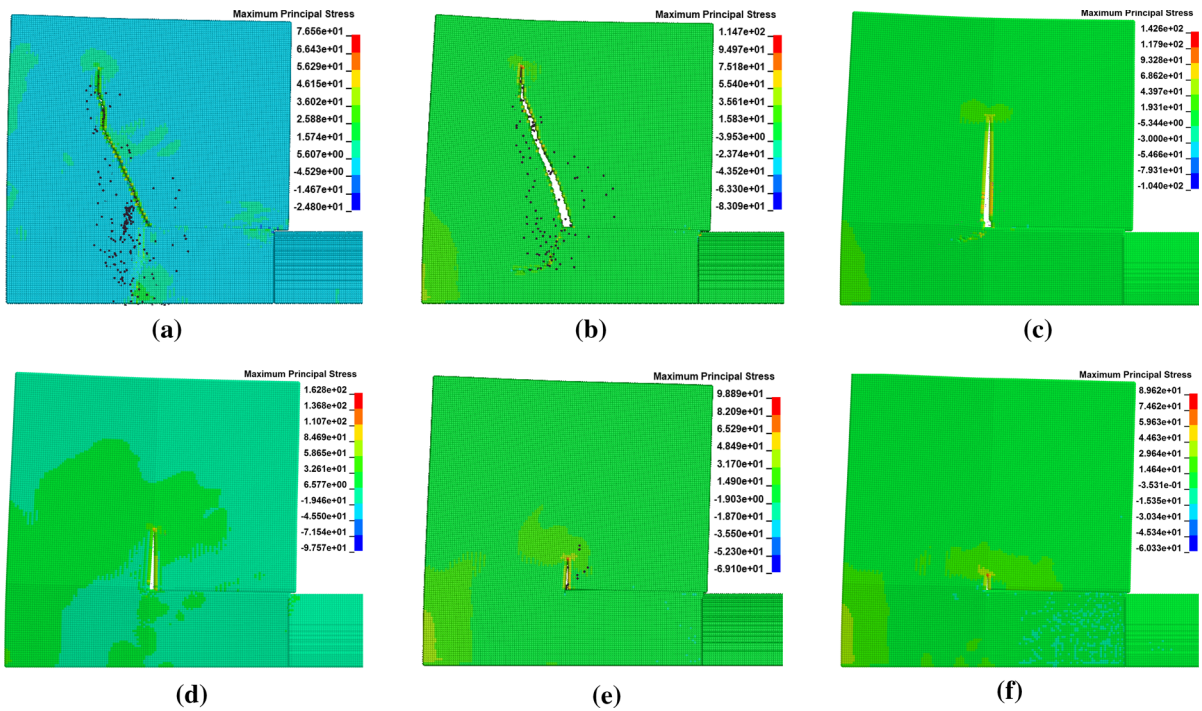


**Fig. 19** Numerical simulation for impact velocity of  $20 \text{ ms}^{-1}$  with different CEPS levels: **a**  $0.5 \times 10^{-2}$ , **b**  $10^{-2}$ , **c**  $2 \times 10^{-2}$ , **d**  $2.9 \times 10^{-2}$ , **e**  $4 \times 10^{-2}$ , and **f**  $5 \times 10^{-2}$

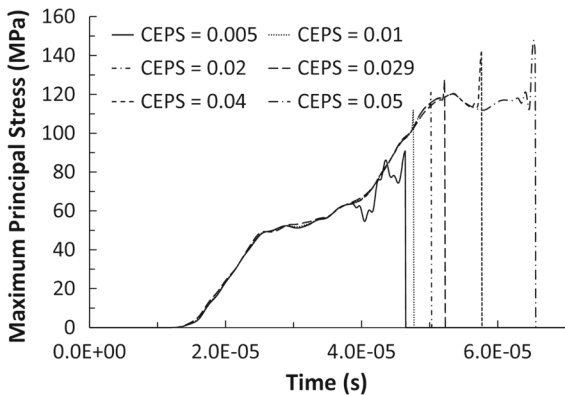


**Fig. 20** Numerical MPS time history in particle 1 of row 2 for various CEPS values. Impact velocity of  $20 \text{ m/s}$

to reproduce the conditions for crack initiation and development. The values of the CMPS and CEPS are tentatively those determined previously, viz. 103 MPa and  $2.9 \times 10^{-2}$  respectively. The failure is accordingly assumed to occur as soon as both CMPS and CEPS are reached. The numerical results are presented in Fig. 21. The latter shows that most of the requirements are met in terms of crack initiation and pattern. Some improvements still need to be brought to

reproduce the correct crack advance as a function of the impact velocity, which is the purpose of the next section.

### 5 Application to RT-PMMA100

It has been experimentally seen that the addition of rubber nanoparticles (in a sufficient concentration) inside a PMMA matrix increases significantly the impact toughness of the resulting material, viz. RT-PMMA100. From the numerical simulation perspective, this gain in ductility implies associating a CEPS-controlled failure criterion to the usual CMPS-controlled failure criterion in order to slow down the crack propagation and accordingly increase the crack resistance. In the following, a design of experiment is conducted to determine the best set of CMPS and CEPS values regarding the experimental results.

#### 5.1 Design of experiment (DOE)

To investigate in a systematic way the combined effects of CMPS and CEPS failure criteria on the

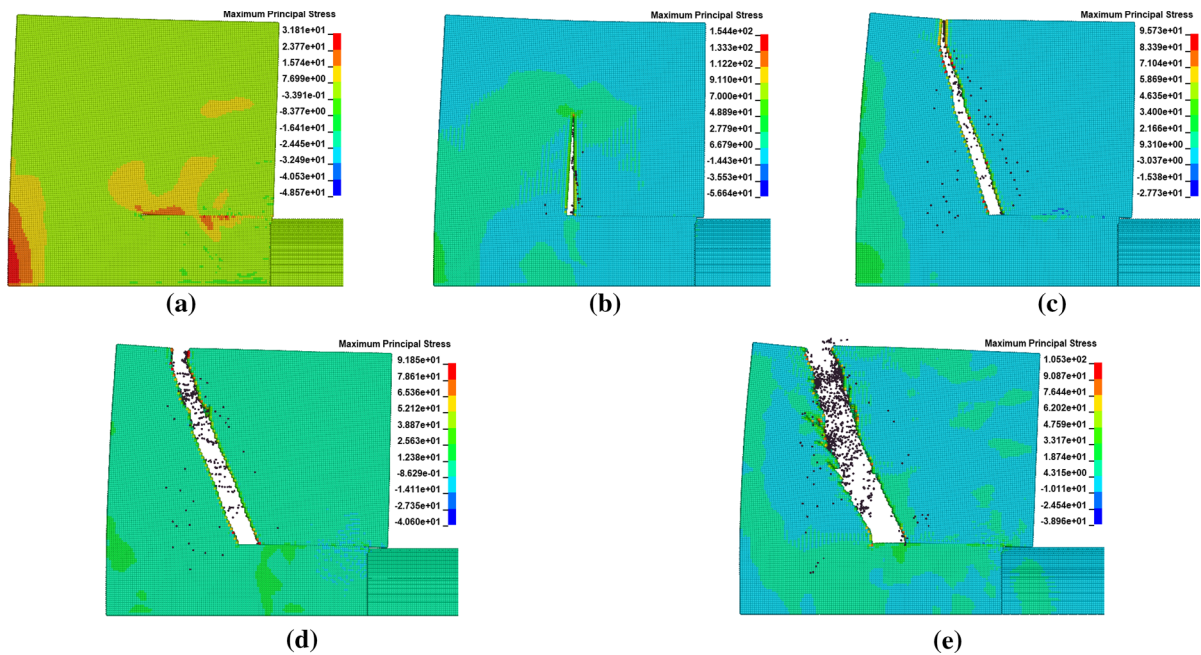


**Fig. 21** Numerical simulation for CMPS = 103 MPa and CEPS =  $2.9 \times 10^{-2}$  for impact velocity of **a** 16, **b** 20, **c** 25, **d** 30, and **e** 40 m/s

fracture of the KW-type doubly-notched plate under impact loading, a factorial design was employed. The factors considered were the material properties of interest, viz. the CMPS and CEPS values, and also an external parameter, viz. the impact velocity. The chosen response variables were the crack advance and propagation angle. Based on the preliminary numerical analysis, it was shown that combining high CEPS with low CMPS or low CEPS with sufficiently high CMPS leads to a finite crack advance. This suggested that the interaction between the two factors would be able to provide an empirical model capable of predicting a suitable combination from the curvature in the response function. Therefore, to be able to investigate such quadratic modelling curvature, central composite design (CCD), see e.g. Montgomery (2013), was employed for the parametric study.

The first step consists of defining a reasonable range for the factors under consideration. The factor bounds are fixed based on the observations of the preliminary numerical analysis as above discussed. Some additional trials are also run in order to check that at the lower limit of the experimental range in terms of impact velocity, the loading does not involve any fracture while at the upper no fragmentation occurs. Factor levels are reported in Table 2 and the design matrix in Table 3. There are accordingly 20 runs to be performed. Yet, since repeated numerical simulations will always yield identical results, only one simulation is required for the run orders 15 to 20.

**Table 2** Factorial design for identification of failure criteria of RT-PMMA 100

Factor	Notation	Factor level	
		Low (−)	High (+)
Critical maximum principal stress CMPS (MPa)	<i>M</i>	90	110
Critical equivalent plastic strain CEPS	<i>F</i>	0.016	0.044
Impact velocity $V_I$ ( $\text{ms}^{-1}$ )	<i>V</i>	19	31

**Table 3** Factor level settings of the DOE CCD matrix

Factor	Run order factor level														
	1	2	3	4	5	6	7	8	9	10	11	12	13	14	15–20
<i>M</i>	90	110	90	110	90	110	90	110	83.182	116.82	100	100	100	100	100
<i>F</i>	0.016	0.016	0.044	0.044	0.016	0.016	0.044	0.044	0.030	0.030	0.0065	0.0535	0.030	0.030	0.030
<i>V</i>	19	19	19	19	31	31	31	31	25	25	25	25	14.91	35.09	25

## 5.2 Results and discussion

### 5.2.1 Overall crack pattern

The numerical simulations with the factors in Table 3 are presented in Fig. 22a–o, corresponding to the run orders 1–15, while their related main crack extensions and propagation angles are reported in Table 4. The lowest crack advance is observed for the run orders three and four, Fig. 22c, d. According to the cases of run orders one vs. two, three vs. four, five vs. six, seven vs. eight, and nine vs. ten, it can be seen that by varying the CMPS levels while maintaining the same CEPS value, the induced crack extension and corresponding propagation angle are generally the same for each pair. On the other hand, they all exhibit crack arrest. This suggests that the crack arrest is not controlled by the CMPS criterion. The predominance of the CEPS level in controlling the crack arrest can be seen in the cases (k) vs. (l), where the CMPS for both cases were 100 MPa but the CEPS levels differ by about 10 times. The effect of impact velocity on the crack propagation is also demonstrated.

Time histories of the MPS in the particles belonging to rows 1 and 2 at the notch tip are plotted in Fig. 23.

According to Fig. 23, depending on the factors set, the failure occurs suddenly during the MPS rising, on the MPS plateau or not at all. The former is particularly seen for the cases three and four which correspond to the CEPS of  $4.4 \times 10^{-2}$ , as compared to cases nine and ten which were assigned with CEPS of  $3 \times 10^{-2}$ . For cases one and two, with CEPS of  $1.6 \times 10^{-2}$ , such a sudden jump is even more insignificant.

### 5.2.2 Analysis of central composite design (CCD)

The effect of the failure criteria and impact velocity on the crack extension is depicted in Fig. 24. As expected, the factor *M*, i.e. CMPS, has no significance effect on the crack extension before crack arrest. In contrast, decreasing the CEPS level will allow for increasing the crack extension while increasing the crack propagation angle. The crack advance increases rather linearly with the impact velocity while tending to reduce the crack propagation angle.

In Fig. 25, the curves show the interactions between *M*-*F* and *M*-*V* for both crack extension and propagation angle. The curves are obviously parallel to each other, suggesting that the interaction effects are not significant. The interaction with significant effect is demonstrated in *F*-*V* where the curves are not parallel to each other. It can be seen that at high level of *V*, increasing the CEPS has no effect but at low level of *V*, increasing the CEPS significantly reduces the crack extension.

## 5.3 Optimised values for the CMPS and CEPS

The contour plots illustrating how the average crack extension and crack propagation angle vary with the failure criteria and impact velocity are presented in Figs. 26, 27, respectively. Based on the contour plots, the region where the experimental results fall are highlighted with red circle, which is 6 mm of crack extension and  $72^\circ$  of propagation angle. From the contour plot of the average crack extension, an estimation of the CMPS and CEPS values are 110–115 MPa and  $4 \times 10^{-2}$ – $5 \times 10^{-2}$ , respectively. On the other hand, contour plots of average propagation angle suggest a range of values for the corresponding CMPS and CEPS as 110–115 MPa and  $3 \times 10^{-2}$ – $5 \times 10^{-2}$ , respectively.

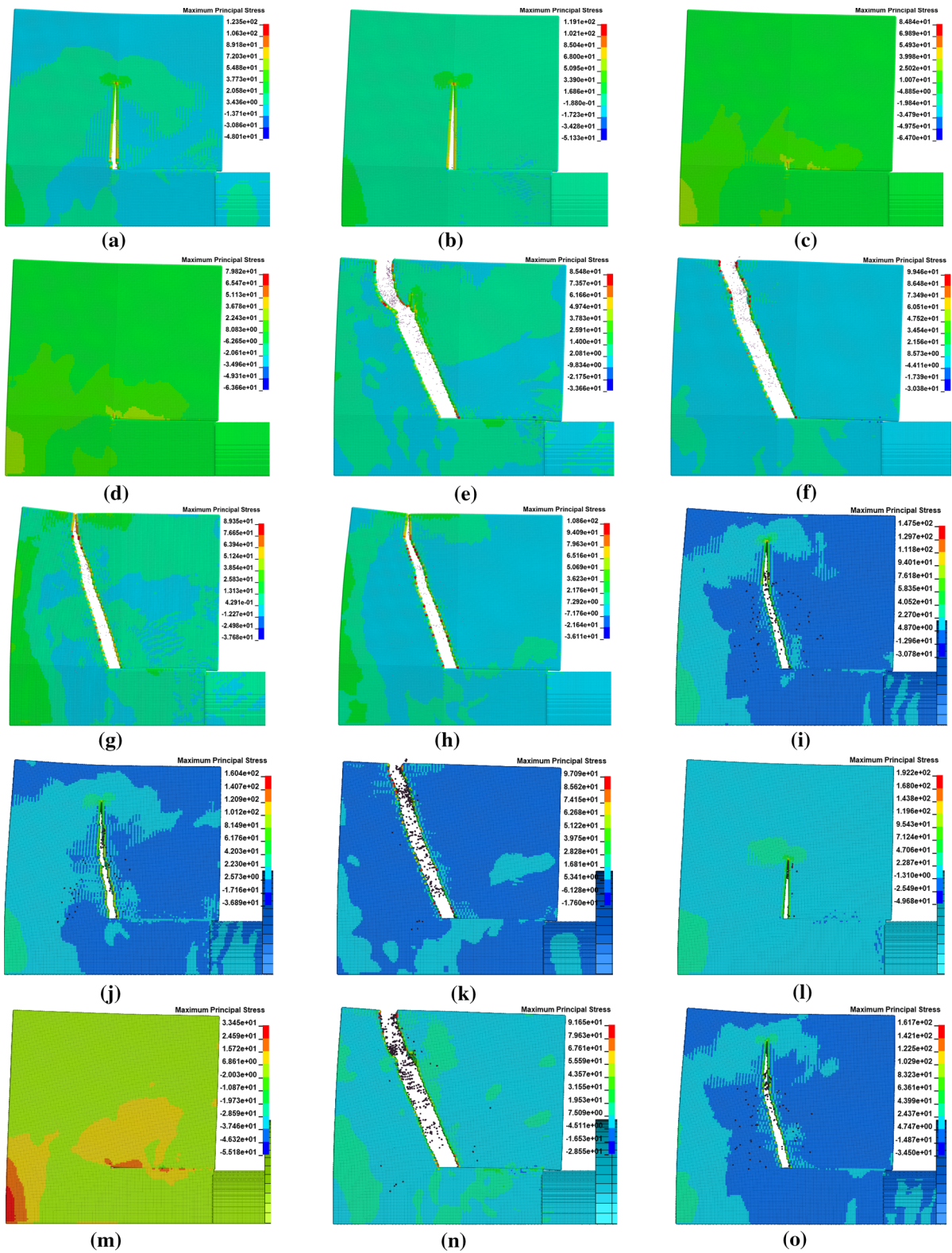


**Fig. 22** Numerical simulation of the KW impact loading according to the design of experiment

**Table 4** Numerical results in terms of main crack extension and propagation angle according to the matrix of the design of experiment

No	Factors			Responses	
	<i>M</i>	<i>F</i>	<i>V</i>	Crack extension (mm)	Propagation angle (°)
1	90	0.0160	19.00	16.0	90
2	110	0.0160	19.00	16.0	90
3	90	0.0440	19.00	1.0	90
4	110	0.0440	19.00	0.5	90
5	90	0.0160	31.00	20.5	65
6	110	0.0160	31.00	20.5	65
7	90	0.0440	31.00	17.0	70
8	110	0.0440	31.00	16.5	69
9	83	0.0300	25.00	15.5	74
10	117	0.0300	25.00	12.5	73
11	100	0.0065	25.00	30.5	69
12	100	0.0535	25.00	11.0	90
13	100	0.0300	14.91	0.0	*
14	100	0.0300	35.09	31.0	66
15	100	0.0300	25.00	14.5	75

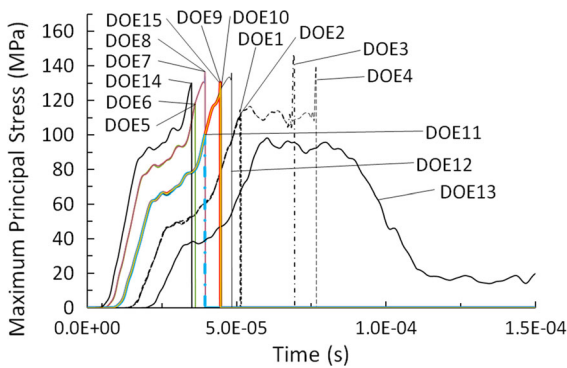


**Fig. 23** Design of experiment. Time histories of the MPS in particle 1 of row 2

Thus, a reasonable estimate for the failure criteria that satisfy both the crack extension and propagation angle are about 115 MPa for critical MPa (corresponding to numerical and not physical dynamic  $K_{Ic} = 29\text{MPa}\cdot\sqrt{m}$ ) and  $5 \times 10^{-2}$  for CEPS. It was found that contour plots of other impact velocities as holding value (not shown here) also demonstrated the same trend. It is noteworthy that this value of 115 MPa as critical MPS equals 2.9 times the average static yield stress of 40 MPa, and then remains within the expected [2;3] range.

The comparison of the experimental and numerical results for this set of CMPS and CEPS is depicted in Fig. 28. It can be seen that the conditions for crack

initiation, the finite crack advance and the crack propagation are fairly reproduced. In particles located near the notches tips, the strain rate is of the order of  $2 \times 10^3 \text{ s}^{-1}$  for 16 m/s and  $5 \times 10^3 \text{ s}^{-1}$  for 40 m/s.

At 25 m/s the magnitude of the early shear loading at the notch tip is not sufficient to initiate the crack formation, and the latter probably results from a predominant Mode I or mixed mode induced by late waves' interaction. For this case, the kink angle is not well reproduced ( $\sim -90^\circ$  numerically against  $\sim -71^\circ$  experimentally) but the crack advance is fairly reproduced.

In the present case, knowing that the wave celerity  $C_{RT-PMMA}$  in the RT-PMMA is close to 1140 m/s, the time the compression wave takes to go from the notch tip to the rear side of the specimen and returns to the notch tip as a release wave is close to  $35 \mu\text{s}$ . This more or less corresponds to the time at the beginning of the plateau in Fig. 11. So, from  $35 \mu\text{s}$ , the notch or crack tip is under mixed Mode II-Mode I loading with one mode being predominant with respect to the other. The analysis of the interaction between the waves coming from the specimen, impacted side (the impedance mismatch involves a long time loading), rear side and upper/lower sides is very complex. One can however propose the following scenarios.

- (1) If the crack initiates within the first  $35 \mu\text{s}$ , it is expected to do it as main crack under pure Mode

**Fig. 24** Design of experiment. Effect of each factor on the crack extension

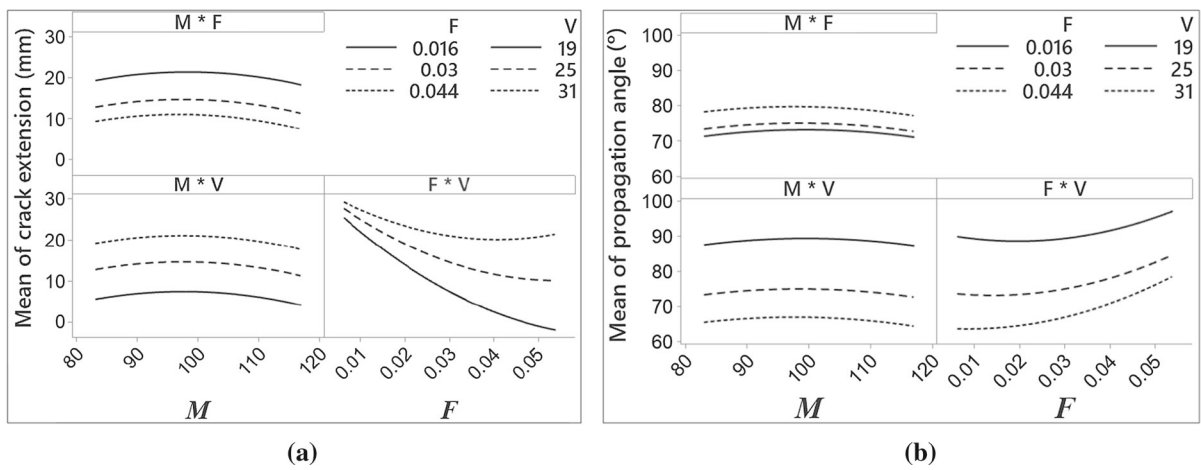
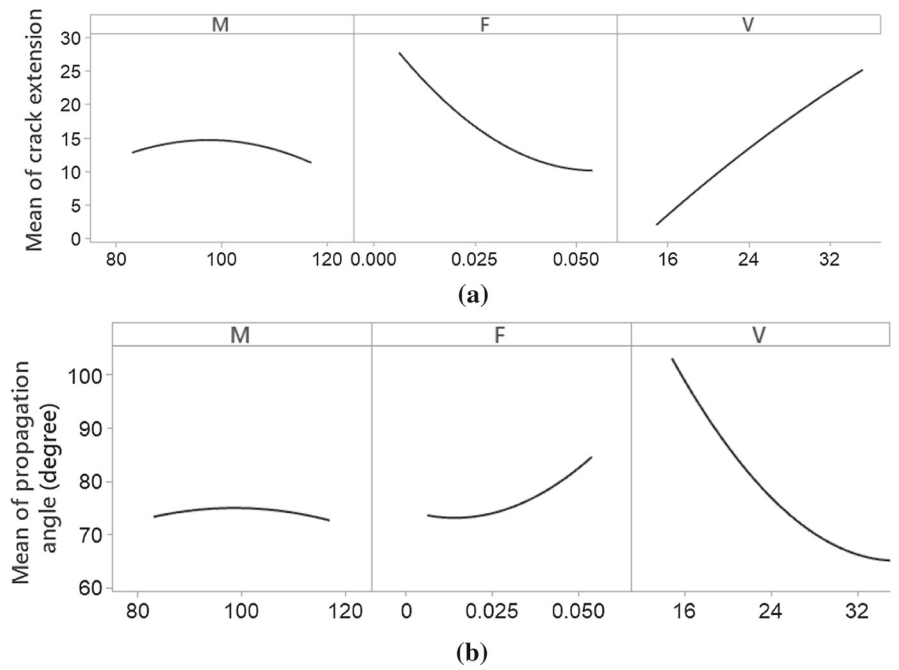


**Fig. 25** Design of experiment. Interaction effects of the factors on crack extension

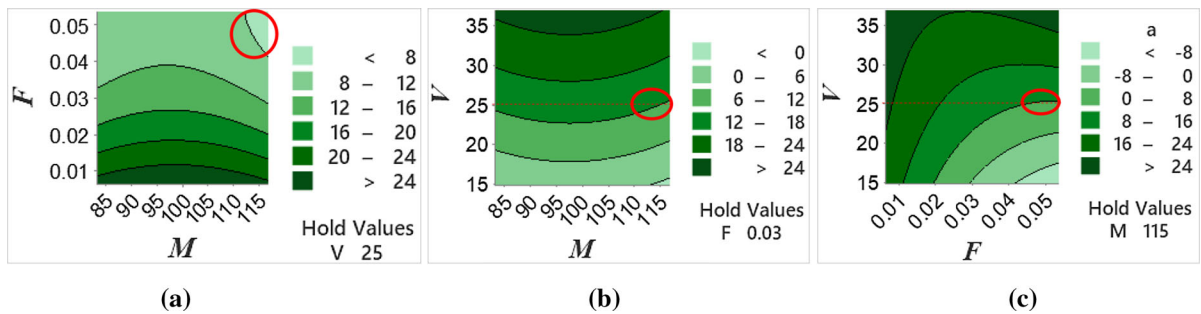


**Fig. 26** Contour plot of average crack extension in terms of a F-M; b V-M; c V-F

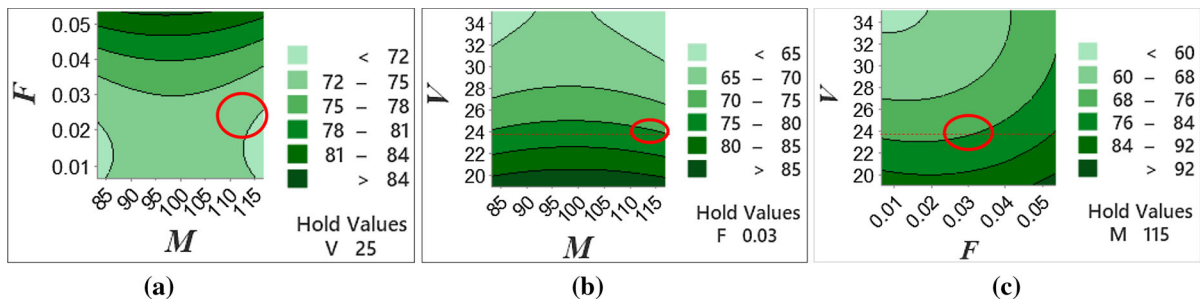


Fig. 27 Contour plot of average crack propagation angle in terms of a F-M; b V-M; c V-F

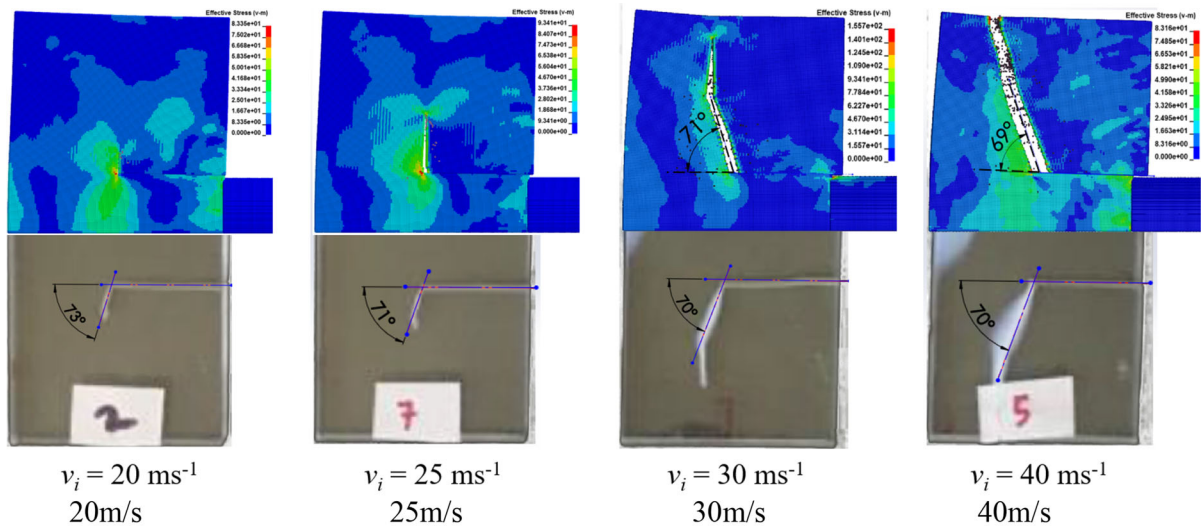


Fig. 28 Numerical simulations considering the optimised CMPS of 115 MPa and CEPS of  $5 \times 10^{-2}$

Table 5 Comparison of averaged measured [after Mat Jali and Longère (2020)] and predicted crack tip speeds for impact velocity of 50 m/s

	Averaged crack tip speed (m/s)
Experimental value	320
Numerical value	335

II shear loading, propagates under Mode II loading as long as the latter is predominant with respect to Mode I, and then propagates as secondary crack under Mode I loading when Mode I becomes predominant.

- (2) Now, if the crack does not initiate within the first 35  $\mu$ s, it is expected to do it as ‘secondary’ crack under Mode I opening loading and propagates under Mode I loading.

### 5.4 Verification of the numerical model

The last step consists in verifying the numerical model by considering a configuration that has not been previously used for the calibration procedure. A numerical simulation has accordingly been conducted at the impact velocity of 50 m/s which is above the threshold impact velocity  $V_T$ . Experimental and numerical, averaged crack tip speeds are reported in Table 5. According to the latter, the numerical model slightly overestimates the crack tip speed with an acceptable error of 4.7%.

### 6 Concluding remarks

The present study aimed to numerically reproduce the crack arrest in impact loaded KW-type doubly-

notched specimens made of shock resistant RT-PMMA100 using SPH method. The ability of critical maximum principal stress- and critical plastic strain-controlled failure criteria, first individually and then combined to reproduce the crack arrest was evaluated by comparison with experimental results. In spite of the overall brittle nature of the PMMA matrix, it was shown that the most pertinent criterion for RT-PMMA is the one expressed in terms of critical plastic strain, as a consequence of the gain in ductility brought by the embedded rubber particles. In practice, the real crack pattern can be reproduced only if the two criteria are used together: the strain-based one to reproduce the crack arrest and propagation angle and the stress-based one to avoid another crack to initiate from the notch tip. Following a design of experiment, an optimised set of values for the critical maximum principal stress and plastic failure strain were found. A good agreement in terms of finite crack advance and arrest (as a function of the impact velocity) and propagation angle is seen between the experimental and numerical results.

In future works, this approach could be applied to higher rubber nanoparticle concentrations (lower concentrations exhibiting no crack arrest within the impact velocity range) in order to potentially relate the latter values to the critical maximum principal stress and critical plastic strain values entering the combined failure criteria. Considering different failure criteria for crack initiation and crack propagation could also constitute an improvement of the methodology.

## References

- Arruda EM, Boyce MC, Jayachandran R (1995) Effects of strain rate, temperature and thermomechanical coupling on the finite strain deformation of glassy polymers. *Mech Mater* 19:193–212
- Batra RC, Gummalla RR (2000) Effect of material and geometric parameters on deformations near the notch-tip of a dynamically loaded prenotched plate. *Int J Fracture* 101:99–140
- Batra RC, Ravinsankar MVS (2000) Three-dimensional numerical simulation of the Kalthoff experiment. *Int J Fracture* 105:161–186
- Batra RC, Lear MH (2004) Simulation of brittle and ductile fracture in an impact loaded prenotched plate. *Int J Fracture* 126:179–203
- Bjerke T, Li Z, Lambros J (2002) Role of plasticity in heat generation during high rate deformation and fracture of polycarbonate. *Int J Plast* 18:549–567
- Chou SC, Robertson KD, Rainey JH (1973) The effect of strain rate and heat developed during deformation on the stress-strain curve of plastics. *Exp Mech* 13(10):422–32
- Combesure A, Coret M, Elguedj T, Cazes F, Haboussa D (2012) Cohesive laws X-FEM association for simulation of damage fracture transition and tensile shear switch in dynamic crack propagation. *Procedia IUTAM* 3:274–291
- Estevez R, Basu S (2008) On the importance of thermo-elastic cooling in the fracture of glassy polymers at high rates. *Int J Solids Struct* 45:3449–3465
- Haboussa D, Elguedj T, Leblé B, Combesure A (2012) Simulation of the shear-tensile mode transition on dynamic crack propagations. *Int J Fract* 178:195–213
- Kalthoff JF (1988) Shadow optical analysis of dynamic shear fracture. *Opt Eng* 27(10):835–840
- Kalthoff JF and Winkler S (1987) Failure mode transition at high rates of shear loading. In: Chiem CY et al (eds) *Impact loading and dynamic behavior of materials*. Informationsgesellschaft Verlag Bremen, pp 185–195
- Kobayashi AS, Mall S (1979) Rapid crack propagation and arrest in polymers. *Polymer Eng Sci* 19–2:131–135
- Lalande L, Plummer CJG, Manson JAE, Gérard P (2006) Microdeformation mechanisms in rubber toughened PMMA and PMMA-based copolymers. *Eng Fract Mech* 73:2413–2426
- Li S, Liu WK, Rosakis AJ, Belytschko T, Hao W (2002) Mesh-free Galerkin simulations of dynamic shear band propagation and failure mode transition. *Int J Solids Struct* 67:868–893
- Li T, Marigo JJ, Guilbaud D, Potapov S (2016) Gradient damage modeling of brittle fracture in an explicit dynamics context. *Int J Numer Methods Eng* 108:1381–1405
- Manar G, Longère P (2019) Crack arrest capabilities of AA2024 and AA7175 aluminum alloys under impact loading. *Eng Fail Anal* 104:1107–1132
- Mat Jali N, Longère P (2020a) Fracture behavior of RT-PMMA under impact loading. *Int J Integr Eng* 12(05):104–107
- Mat Jali N, Longère P (2020b) Experimental investigation of the dynamic fracture of a class of RT-PMMA under impact loading. *Int J Fracture* 225:219–237
- Mazidi MM, Berahman R, Edalat A (2018) Phase morphology, fracture toughness and failure mechanisms in supertoughened PLA/PB-g-SAN/PMMA ternary blends: a quantitative analysis of crack resistance. *Polym Test* 67:380–391
- Milios J, Papanicolaou GC, Young RJ (1986) Dynamic crack propagation behaviour of rubber-toughened poly(methyl methacrylate). *J Mater Sci* 21:4281–4288
- Montgomery DC (2013) *Design and analysis of experiments*, 8th edn. Wiley, New York
- Nasraoui M, Forquin P, Siad L, Rusinek A (2012) Influence of strain rate, temperature and adiabatic heating on the mechanical behaviour of poly-methylmethacrylate: experimental and modelling analyses. *Mater Des* 37:500–509
- Needleman A, Tvergaard V (1995) Analysis of a brittle-ductile transition under dynamic shear loading. *Int J Solids Struct* 32–17(18):2571–2590

- Pan Z, Sun B, Shim VPW, Gu B (2016) Transient heat generation and thermo-mechanical response of epoxy resin under adiabatic impact compressions. *Int J Heat Mass Transf* 95:874–889
- Ravi-Chandar K, Lu J, Yang B, Zhu Z (2000) Failure mode transitions in polymers under high strain rate loading. *Int J Fract* 101:33–72
- Raymond S, Lemiale V, Ibrahim R, Lau R (2014) A mesh free study of the Kalthoff-Winkler experiment in 3D at room and low temperatures under dynamic loading using viscoplastic modelling. *Eng Anal Boundary Elem* 42:20–25
- Rittel D (1999) On the conversion of plastic work to heat during high strain rate deformation of glassy polymers. *Mech Mater* 31(2):131–139
- Roux E, Longère P, Cherrier O, Millot T, Capdeville D, Petit J (2015) Analysis of ASB assisted failure in a high strength steel under high loading rate. *Mater Des* 75:149–159
- Sih GC (1974) Strain energy density factor applied to mixed mode crack problems, *Int. J Fract* 10–3:305–321
- Sih GC (1991) Mechanics of fracture initiation and propagation. In: Sih GC (ed) *Engineering application of fracture mechanics*. Springer, New York
- Song JH, Areias PMA, Belytschko T (2006) A method for dynamic crack and shear band propagation with phantom nodes. *Int J Numer Methods Eng* 67:868–893
- Wang J, Zhang X, Jiang L, Qiao J (2019) Advances in toughened polymer materials by structured rubber particles. *Prog Polym Sci* 98:101160
- Weerasooriya T, Moy P, Cheng M, Chen W (2006) Fracture toughness of PMMA as a function of loading rate. In: *Proceedings of the 2006 SEM Annual Conference on Experimental Mechanics*, St. Louis, MO, pp 1–8
- Yreux E (2018) MLS-based SPH in LS-DYNA for increased accuracy and tensile stability. In: *15th International LS-DYNA Users Conference*
- Zehnder AT (2012) Fracture mechanics. In: Pfeiffer F, Wriggers P (eds) *Lecture notes in applied and computational mechanics*, vol 62. Springer, New York
- Zhou M, Rosakis AJ, Ravichandran G (1996a) Dynamically propagating shear bands in impact-loaded prenotched plates-I. Experimental investigations of temperature signatures and propagation speed. *J Mech Phys Solids* 44:981–1006
- Zhou M, Rosakis AJ, Ravichandran G (1996) (1996b), Dynamically propagating shear bands in impact-loaded prenotched plates-II. Numerical simulations. *J Mech Phys Solids* 44:1007–1032
- Zhou X, Wang Y, Qian Q (2016) Numerical simulation of crack curving and branching in brittle materials under dynamic loads using the extended non-ordinary state-based peridynamics. *European Journal of Mechanics A/Solids* 60:277–299

**Publisher's Note** Springer Nature remains neutral with regard to jurisdictional claims in published maps and institutional affiliations.